CHALMERS
UNIVERSITY OF TECHNOLOGY

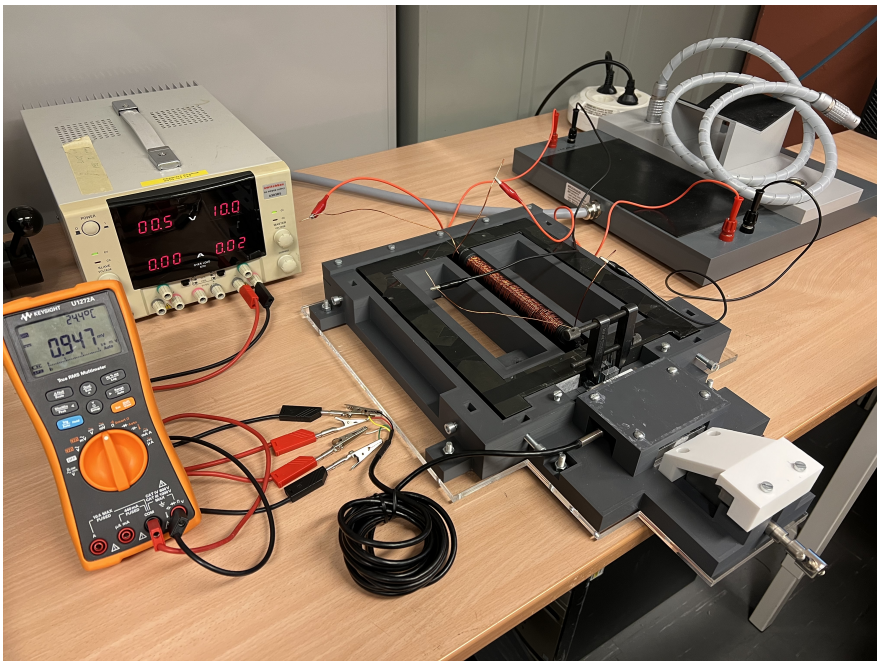

Development of Magnetizing Frame for Analyzing Effects of Compressive Stress on Magnetic Properties of Electrical Steel

Master's Thesis in Sustainable Electric Power Engineering and Electromobility

TIM LINDBERG
ZIJIE LIN

Department of Electrical Engineering
Division of Electric Power Engineering
CHALMERS UNIVERSITY OF TECHNOLOGY
Gothenburg, Sweden 2023
Master's Thesis

Master's Thesis

Development of Magnetizing Epstein Frame for Analyzing Effects of Compressive Stress on Magnetic Properties of Electrical Steel

TIM LINDBERG
ZIJIE LIN

CHALMERS
UNIVERSITY OF TECHNOLOGY

Department of Electrical Engineering
Division of Electric Power Engineering
Chalmers University of Technology
Gothenburg, Sweden 2023

Development of Magnetizing Epstein Frame for Analyzing Effects of Compressive Stress on Magnetic Properties of Electrical Steel
TIM LINDBERG
ZIJIE LIN

Supervisor: Rishabh Raj, Volvo Cars Corporation
Examiner: Torbjörn Thiringer, Electrical Power Engineering

Master's Thesis
Department of Electrical Engineering
Division of Electric Power Engineering
Chalmers University of Technology
SE-412 96 Göteborg
Sweden
Telephone +46 (0)31 772 1000

Typeset in Latex
Chalmers Bibliotek, Reproservice
Göteborg, Sweden, 2023

Development of Magnetizing Epstein Frame for Analyzing Effects of Stresses on Magnetic Properties of Electrical Steel
TIM LINDBERG
ZIJIE LIN
Department of Electrical Engineering
Division of Electric Power Engineering
Chalmers University of Technology

Abstract

As electric motors are becoming more widely used within the automation industry, assessing the impact of different factors on electric machine efficiency is essential, both from an economic and environmental aspect. In vehicles, stator housings are fitted to stators of rotating machines using a joint fit that generates compressive stress throughout the stator, affecting magnetic properties and losses of the stator material. In this thesis work, a magnetizing frame for measuring magnetic properties of electrical steel when subjected to compressive stress has been developed. The developed frame showed good accuracy when compared to standardized equipment and was successful in applying compressive stress of up to 60.6 MPa to electrical steel samples and measuring their magnetic properties. It was found that for frequencies in the range 50 - 1000 Hz and compressive stress in the range of 10.3 - 60.6 MPa, the iron losses of NO-25 1350H increased with 15% - 74.88% depending on level of magnetization. Furthermore, changes in magnetization behavior and hysteresis loop shapes of the material were observed.

The measured stress dependent magnetic properties were utilized to create a stator material for a Finite Element Method (FEM) 2D-design of an Interior Permanent Magnet (IPM) motor with stator housing fitted to the stator through a joint fit. Loss increase in the stator due to joint fit was found to be highest in the stator yoke and impact on machine efficiency was highest at lower machine torque. For a case with lower compressive stress of approximately 16 MPa in the yoke, efficiency of the machine at different operation points decreased with up to 0.74% and for a case with higher compressive stress of approximately 31 MPa in the stator yoke, efficiency of the machine decreased with up to 1.3%. Measuring effects of tensile stress on the material and utilizing frame measurements in a 3-dimensional model were identified as potential future works.

Keywords: Magnetization, Hysteresis loop, Compressive stress, Single-sheet tester(SST), Joint fit, Electrical steel, Interior Permanent Magnet(IPM), Finite Element Method (FEM).

Sammanfattning

Elekriska motorer används allt mer inom automationsindustrin, vilket medför att förståelsen för effekterna av olika faktorer på verkningsgraden hos elektriska maskiner är väsentlig, både från ett ekonomiskt och miljömässigt perspektiv. I fordon monteras statorhus till statorer i roterande maskiner genom en fogpassning som generar påfrestningar i form av kompression i statorn, vilket påverkar statormaterialets magnetiska egenskaper och förluster. I detta examensarbete har en magnetiseringsram, inspirerad av en Single Sheet Tester (SST), för mätning av magnetiska egenskaper hos elektriskt stål som utsätts för kompression utvecklats. Den utvecklade ramen visar god nogrannhet vid jämförelse med standardiserad utrustning och lyckades applicera kompression upp till och med 60.6 MPa på elektriska stålprov samt mäta materialets magnetiska egenskaper. Det upptäcktes att för frekvenser i området 50 - 1000 Hz och kompression i området 10.3 - 60.6 MPa ökade järnförlusterna hos NO-25 1350H med 15% - 74.88% beroende på magnetiseringsnivå. Utöver detta observerades även förändringar i materialets magnetiseringsbeteende och form på dess hysteresloopar.

De uppmätta påfrestningsberoende magnetiska egenskaperna användes för att skapa ett stator material för en Finita Element Metod (FEM) 2D-design av en inre permeanentmagnets(IPM)motor med statorhus monterat till statorn genom en fogpassning. Det upptäcktes att förlustökningen i statorn var högst i statoroken och att påverkan på maskinens verkningsgrad var högst vid lågt vridmoment. För ett fall med låg kompression runt 16 MPa i statoroken, minskade verkningsgraden i maskinen vid olika operationspunkter med upp till och med 0.74 % och för ett fall med högre kompression runt 31 MPa i statoroken minskade verkningsgraden i maskinen med upp emot 1.3 %. Mätning av effekten av uttöjning på materialet och användandet av mätvärden från ramen i en 3-dimensionell modell identifierades som möjliga framtida arbeten.

Keywords: Magnetisering, Hysteresloop, Kompression, Single-sheet tester(SST), Fogpassning, Electrical steel, Inre permanentmagnets(IPM)motor, Finita element metoden (FEM).

Acknowledgements

Studying at Chalmers University of Technology has been a remarkable experience we will always treasure. The friendships formed and memories created during our time here will remain with us always.

We would like to give special thanks to our manager at Volvo cars, Anders Thulin, for providing us with the opportunity to conduct our master thesis at the company. We would also like to give thanks to the rest of our team at Volvo Cars who have always been eager to lend us a hand when we have been struggling. We would also like to thank our examiner from Chalmers, Torbjörn Thiringer, for the support and feedback he has provided during this thesis work.

We would also to show our sincere gratitude to Sima Soltanipour for assisting us with the equipment, and to Victor Lidskog for many fruitful discussions regarding our respective projects. We also want to give our deepest appreciation to our supervisor Rishabh Raj. He has guided us throughout the thesis, providing us with great support, guidance and enthusiasm. Furthermore, he has also provided us with great knowledge and helped us better realise what it means to be an engineer. We wish him all the best in his future endeavours.

A special thanks to CASE lab and their members for providing us with equipment, materials and guidance, without them, building our frame would have been difficult. We must also give thanks to the Department of Electrical Engineering at Chalmers Institute of Technology for allowing access to their Brockhaus equipment, as it provided us with great convenience when conducting this thesis.

Last, we would like to thank our families for the encouragement and support they have shown throughout this journey.

Tim Lindberg and Zijie Lin, Göteborg, Sweden, 2023

Contents

1
Introduction

1.1 Background

Policies aimed at reducing greenhouse gas emissions and air pollution from transportation are being implemented by governments worldwide, and electric vehicles are widely viewed as a crucial component in achieving these objectives. Consequently, numerous countries have set ambitious targets for the adoption of electric vehicles in the coming years. On February 14, 2023, the European Parliament adopted the European Commission and European Council's agreement on zero emissions for new fuel cars and small trucks in Europe by 2035 [1]. This agreement signifies that the transformation of the automotive industry from fuel vehicles to pure electric vehicles will be accelerated.

The standard electrical vehicles (EV)s, also known as a battery-powered electric vehicles (BEV)s, are expected to play an increasingly important role in the future automobile market. Many traditional automakers are also investing heavily in BEVs, with plans to launch new electric and hybrid models in the coming years. This includes companies such as General Motors, Ford, Volvo, and Volkswagen, which have set ambitious targets for the electrification of their vehicle fleets.The driving motor is one of the most critical components of a new energy vehicle, and its efficiency is essential for producing high-performance vehicles. [2] shows that 86% of manufacturers have chosen Permanent Magnet Synchronous Motors (PMSM)s as the driving motor for their electric vehicle products, thus improving the efficiency of PMSMs is essential.

Non-oriented electrical steel is the preferred material for the manufacturing of stators and rotors of rotating electrical machines. The quality of the silicon steel sheet accounts for approximately half of the driving motor's weight and about one-fifth of its cost. Therefore, the quality of the silicon steel sheet has a large impact on the performance of the driving motor and the entire vehicle [3]. As a result, major car manufacturers and steel companies worldwide have increased their research efforts on non-oriented silicon steel sheets. Major steel companies, such as Japan's Nippon Steel, South Korea's POSCO, and China's Baowu Steel, have developed different grades of cold-rolled non-oriented silicon steel sheets [4].

1.2 Problem

Precise estimation of losses in electric motors is crucial for optimizing the design and configurations of the motor, with the aim of ensuring a high motor efficiency. When the motor is operated, the electrical steel in the stator is exposed to compressive stress due to the installation techniques used when fitting the stator housing to the stator. These stresses alter the microscopic structure of the steel material and, thus, change the magnetic properties of the stator material. This leads to a change in iron losses in the stator, which impacts the efficiency of the motor [5]. This is the problem that this thesis aims to investigate further.

1.3 Purpose

The objective of this thesis is to construct a magnetic frame of high durability capable of investigating the impact of unidirectional compressive stress on the iron losses of electrical steel sheets. Furthermore, this thesis also aims to study the implications of the magnetic frame results by running simulations of a rotating machine experiencing compressive stress in a FEM-based software.

1.4 Scope

The main focus of this thesis is to investigate the influence of compressive stress on materials used in stator design of electrical motors. In order to reduce the complexity of the design, there will not be any built-in function in the frame that allows for applying tensile stresses to the test samples. Furthermore, when compressive stress is applied to the test samples it is assumed that the stress is uniform throughout the samples.

Simulations in FEM-based software will run for a 2D-model of a rotating machine, since generating stress distribution for a 3D-model requires complex modelling of the stress distribution that the time limitations of the thesis do not allow for.

1.5 Outline

The outline of the thesis is that after the current chapter, where the introduction of the thesis project is provided, the next chapter will provide a theoretical background regarding electrical steel, magnetizing frames and principal stress, as well as some implications of previous works. Chapter 3 presents the design of the frame and the measuring setup used in the thesis. In chapter 4 and 5, test results from the developed frame and results from the FEM-based simulations, respectively, are presented. Lastly, discussions regarding the methodology used in the thesis, as well as possible improvements and future works, are the focus of chapter 6, before drawn conclusions from the thesis project are given in chapter 7.

2
Theory

2.1 Electrical steel

Electrical steel is an alloy consisting of iron and up to 6.5% of silicon. Electrical steel is widely used in electrical equipment, such as rotating machines and transformers, due to the high magnetic permeability and electrical resistivity of silicon that leads to low iron core losses. The steel is rolled into thin sheets that are stacked together to form the core. Even if higher silicon content decreases core losses, the most commonly used electrical steel grade today consists of 3% silicon (Fe-3%Si steel). At higher grades of silicon, saturation magnetization of electrical steel decreases and it becomes more brittle, leading to challenges when rolling it into thin sheets [6].

There are two different classifications of electrical steel; grain-oriented electrical steel and non-oriented electrical steel.

2.1.1 Grain-oriented steel

Grain oriented steel usually has a silicon grade of 3% and is processed in a way so that its magnetic properties are optimised in the rolling direction, RD. Thus, grain oriented steel is anisotropic, since it has different magnetic properties depending on the direction of magnetisation. It is widely used in static electric equipment such as transformers, where it is desirable for the steel to have ideal magnetic properties in a specific direction even at the expense of poor properties in other directions, because you can ensure that the flux is flowing in the rolling direction.

2.1.2 Non-oriented steel

Non-oriented steel usually has a silicon content of 0.5 - 3.25%. Non-oriented steel, as opposed to grain-oriented steel, is isotropic and has similar magnetic properties regardless of direction of magnetisation. Non-oriented steel is therefore widely used in rotating machines where the direction of magnetisation changes continously. Also, the production process of non-oriented steel is not as complex as the production process of grain-oriented steel, which is why non-oriented steels have lower costs than grain-oriented steels.

2.1.3 Domain structure

Ferromagnetic materials consist of many domains and within each domain magnetization is uniform. The region in between domains, where polarization changes direction, is known as a domain wall. When ferromagnetic materials are exposed to an electric field domains with favorable polarisation orientation will increase in size while less favorable domains will shrink, causing the domain walls to move. This domain wall dynamic is known as domain wall motion. In [7] it was found that in grain-oriented steel, compressive stress favours other domains than the applied electrical field, which impacts domain wall motion and pushes magnetization to higher fields. Furthermore, in [8] this was also studied for non-oriented steel where the results of the study also showed compressive stress favouring other domains, pushing magnetization to higher fields.

2.1.4 Iron Losses

The total losses of electrical steel cores are composed of eddy losses, hysteresis losses and excess losses.

2.1.4.1 Eddy losses

When laminations are subjected to alternating fluxes, circulating eddy currents are induced in the laminations according to Faraday's law of induction. These eddy currents oppose the change of flux, attempting to force the magnetic field to the outer edges of the lamination. This skin effect is given by

$$\delta = \sqrt{\frac{\rho}{\mu \pi f}} \tag{2.1}$$

where δ is skin depth, ρ is electrical resistivity, μ is total magnetic permeability and f is frequency. As the magnetic field is forced to the outer edges of the lamination, eddy current losses are created in the form of heat in the iron core [9].

Iron cores are composed of thin, insulated electrical steel sheets stacked together in order to oppose the effects of eddy currents and reduce eddy losses. Under the assumption that flux distribution is uniform throughout the lamination, eddy losses can be calculated using

$$P_e = k_e B_p^2 f^2 = \frac{\pi^2 d^2 B_p^2 f^2}{6\rho} \tag{2.2}$$

where k_e is the eddy loss coefficient, B_p is peak flux density and d is thickness of the lamination.

2.1.4.2 Hysteresis losses

When electrical steel is first magnetized it follows a virgin curve up until the point of flux saturation. At saturation, or at some point just before it, the microscopic structure of the material changes due to domain wall motion. Because of this, the magnetization of electrical steel is not reversible by simply removing the applied

electric field as seen in Figure 2.1. When the field is removed entirely, there is still a remnant magnetization, B_r, present (BH-curve no longer follows the virgin curve). In order to demagnetize electrical steel entirely, a coercive field, H_c, is needed in the reverse direction.

If the reverse current is increased until the electrical steel is fully magnetized in the opposite direction, domain wall motion will occur again. When the field is removed, there will be remnant magnetization left in the reverse direction.

As seen in Figure 2.1, as electrical steel is magnetized and demagnetized its BH-characteristics form a closed curve called a hysteresis loop. The total iron loss is the energy required to perform a full cycle of magnetizing and demagnetizing, and it is lost in the form of heat. Hysteresis loss is the energy required for this process when $f \to 0$.

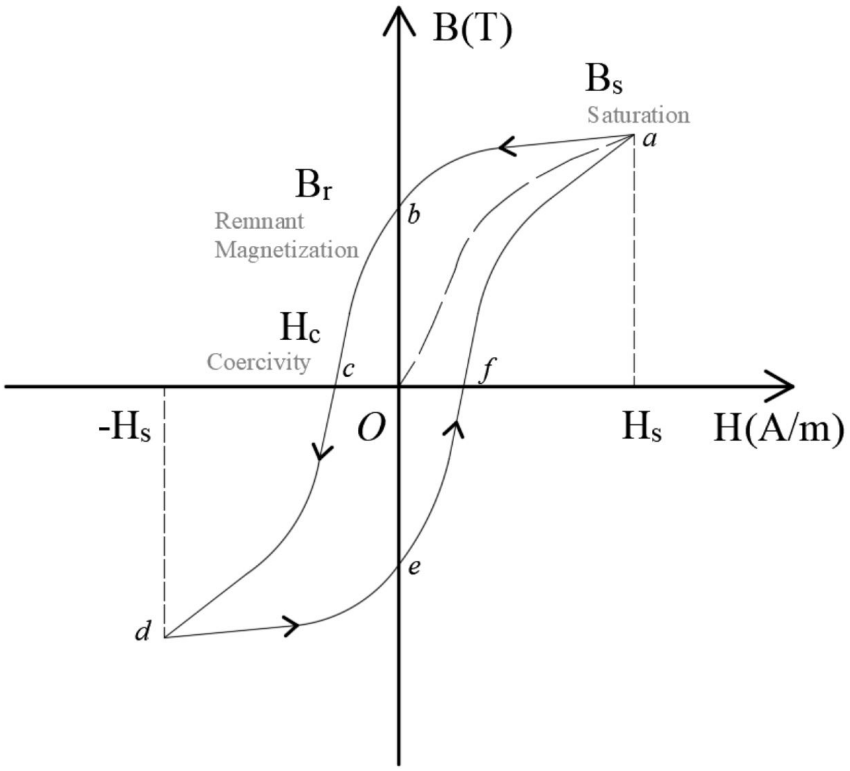

Figure 2.1: Magnetic hysteresis loop of electrical steel

Hysteresis loss can be calculated as

$$P_h = k_h B_p^2 f \tag{2.3}$$

where k_h is the hysteresis loss coefficient.

2.1.4.3 Excess Losses

The final loss component of the total iron loss is excess loss, which is caused by small eddy currents generated by domain wall motion. From Bertotti's loss theories, equations have been derived in previous studies to calculate excess loss [10, 11, 12]

$$P_{ex} = 2B_p f(\sqrt{n_0^2 V_0^2 + \frac{2\pi^2 GAV_0 B_p f}{\rho}} - n_0 V_0) \tag{2.4}$$

where n_0 is number of simultaneously active magnetic objects (MOs) in the material at the quasi-static state ($f \to 0$), G is a constant ≈ 0.1356, A is cross section area of the lamination and V_0 is a magnetic field that controls the increase in MOs caused by the excess dynamic field acting on the MOs. This impact of V_0 can be seen in

$$n(t) = n_0 + \frac{H_{ex}(t)}{V_0} \tag{2.5}$$

where $n(t)$ is the time varying number of active MOs and H_{ex} is the excess field acting on the MOs. In [11] it was found that, based on measured results, for non-oriented steels n_0 can be neglected, which suggests that the impact of the external field on the number of MOs is much higher than that of n_0 in non-oriented steel. (2.4) can then be simplified to

$$P_{ex} = k_{ex} B_p^{1.5} f^{1.5} = \sqrt{\frac{8\pi^2 GAV_0}{\rho}} B_p^{1.5} f^{1.5} \tag{2.6}$$

where k_{ex} is the excess loss coefficient.

2.1.4.4 Loss models

Several loss models have been developed in previous studies to separate loss components from total iron losses in electrical steel. While some loss models neglect excessive losses due to their low contribution to total losses, it has been shown that excessive losses increase due to compressive stress and should therefore not be neglected in a loss study focusing on stress impact. Bertotti's model [13] for loss separation, unlike models derived before it, does not neglect the contribution of excess losses in total iron loss. Bertotti's loss model is

$$P_{tot} = P_e + P_h + P_{ex} \tag{2.7}$$

where P_e, P_h and P_{ex} can be calculated using (2.2), (2.3) and (2.6) respectively. Bertotti's model can be used to derive expressions for total loss as function of stress.

2.2 Magnetizing frames

Magnetizing frames are used to measure the magnetic properties of electrical steel sheets at operating frequencies in order to determine losses and compatibility of the sheets. In magnetizing frames, a primary and secondary winding is wound

around the electrical steel sheets in order to be able to magnetize the samples. The magnetic properties of the sample are determined by measuring flux density and field strength of the sample. Magnetic field strength is determined by tracing the magnetizing current in the primary winding and using Ampere's law[14],

$$H = \frac{N_1 I_1}{l_m} \tag{2.8}$$

where H is magnetic field strength, N_1 is number of turns of the primary winding, I_1 is magnetizing current in the primary winding and l_m is magnetic path length.

Flux density is determined by sensing and integrating the voltage of the secondary voltage according to

$$B = -\int \frac{V_2(t)dt}{N_2 A} \tag{2.9}$$

where B is flux density, $V_2(t)$ is voltage of the secondary winding, N_2 is number of turns in secondary winding and A is cross section area enclosed by the windings. Furthermore, total specific loss of the sample can be determined using

$$P_{loss} = \int \frac{fH(B)dB}{\rho} \tag{2.10}$$

where f is operation frequency and ρ is material density.

2.2.1 Single sheet tester

The Single Sheet Tester (SST) is standardized in IEC Standard 60404-3[15]. A single electrical sample sample is placed within a coil with a primary and secondary winding. Two U-shaped yokes made of highly permeable ferromagnetic material with low iron losses intersect the sample from both sides at the outer edges, creating a magnetic path for the flux (as seen in Figure 2.2). The yoke material is chosen to ensure that losses in the yoke can be neglected so that all measured losses are occurring in the steel sheet.

2.2.2 Epstein frame

The 25 cm Epstein frame, or Epstein square, is a magnetizing frame that is characterized according to IEC Standard 60404-2 [14]. The Epstein frame consists of four branches of equal length and equal cross section area that, together, form a square. Each branch has a primary winding on the outside and secondary winding on the inside wrapped around the same core, so that each branch forms an unloaded transformer. The number of turns of the winding should be equal for each coil. The primary windings of the coils are connected in series, as are the secondary windings which can be seen in Figure 2.3.

An equal number of samples are inserted in each branch, with samples overlapping in the corners of the frame as seen in Figure 2.4. A force of up to 1 N can be applied

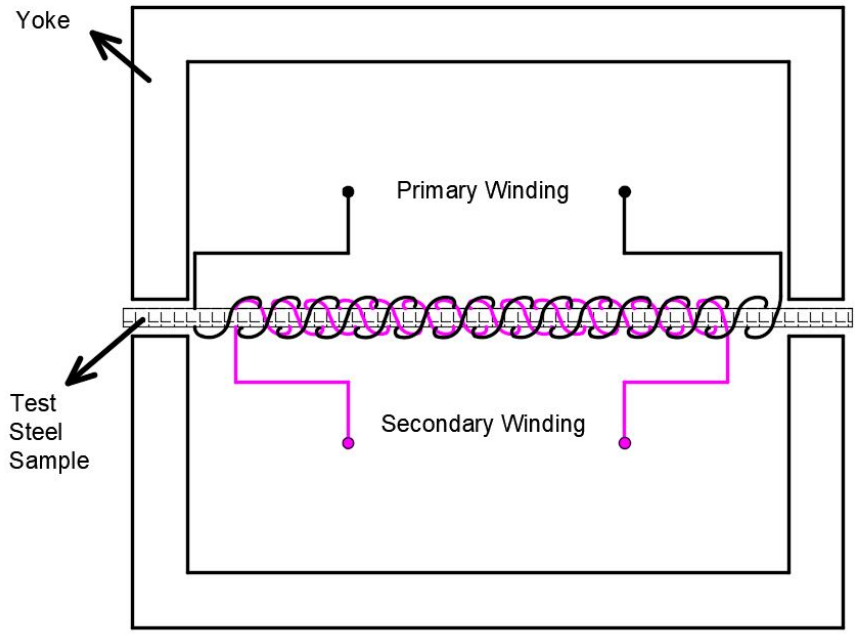

Figure 2.2: Single sheet tester

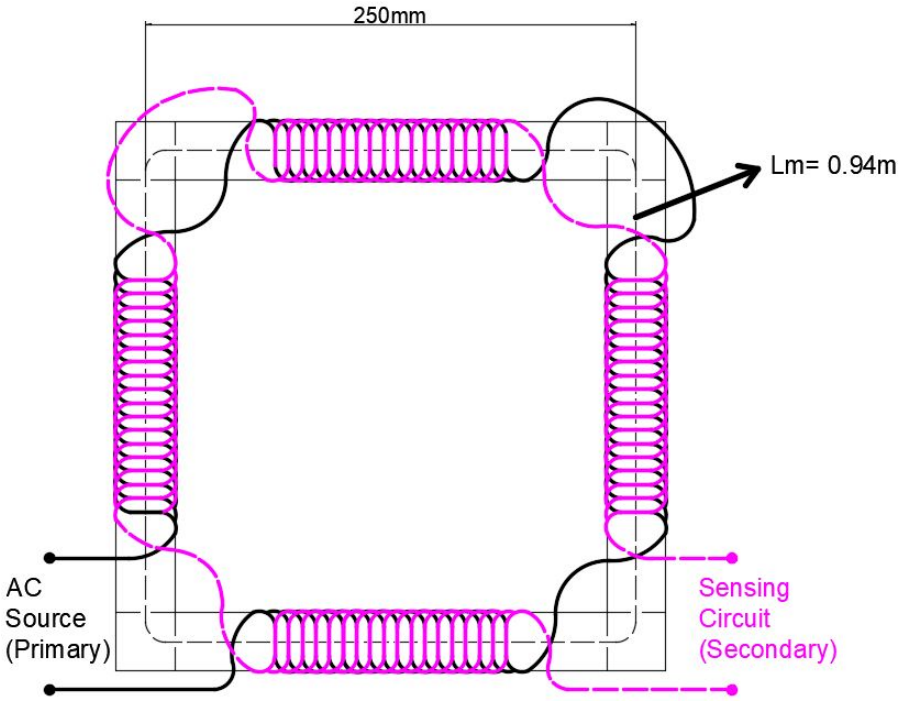

Figure 2.3: Model of standard 25 cm Epstein frame

in each corner to minimize space in between the samples and thus reduce leakage air flux. A mutual inductor is added in the center of the frame to further compensate the leakage air flux, where the primary winding of the mutual inductor is connected

in series with the primary winding of the frame and the secondary winding of the mutual inductor is connected in series opposition with the secondary winding of the frame.

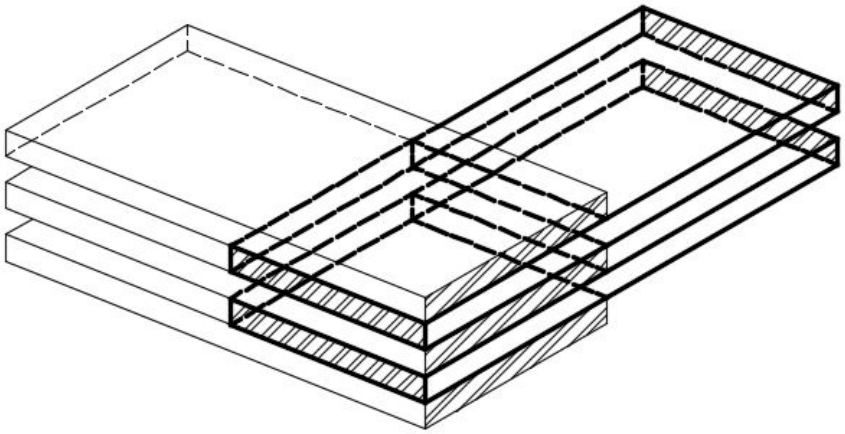

Figure 2.4: Model of overlapping corners in Epstein frame

The advantage of the Epstein frame, in comparison to the SST, is that samples are tested in multiples of four allowing for a larger sample size. The disadvantage of the Epstein frame when compared to the SST is that there is more leakage air flux in the frame due to the overlapping corners.

2.2.3 Rotational single sheet tester

The Rotating Single Sheet Tester(RSST) is designed to perform unidirectional alternating magnetic measurements, as well as circular and rotating magnetization at different angles, θ, with respect to the rolling direction (direction of easy magnetization), in order to replicate flux density observed at various locations within electrical machines. The magnetic configuration of the RSST is illustrated in Figure 2.5 [16].

The yokes are structured as cross-shaped arms, allowing magnetization in both x and y directions, while maintaining a small airgap between the fixed sample positioned in the center. The flux paths are collectively closed over the rectangular outer section of the yoke. The required magnetic field for magnetization of the sample is generated by exciting windings that are fixed on the four arms of the yoke. The magnetic flux density is measured by two orthogonal windings that are inserted into the sample through drilled holes, and the excitation current is adjusted to control the measured flux density. Two sets of H-coils per direction are positioned at a fixed distance below the sample. By measuring the magnetic field strengths at different distances from the sample the vector field strength acting on the sample can be determined through extrapolation.

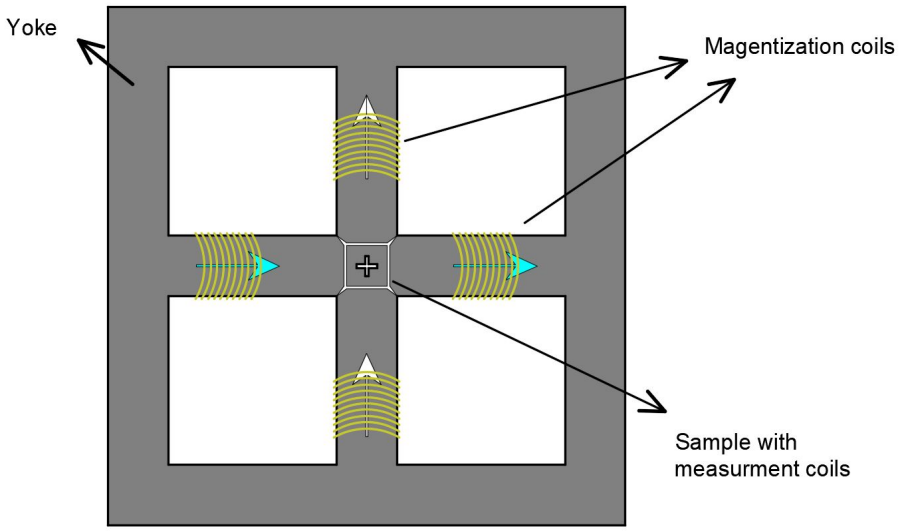

Figure 2.5: Rotational single sheet tester

2.3 Stress

Electrical steel used in electric motors can experience changes in their properties over their lifespan due to the presence of magneto-mechanical coupling, both during the manufacturing process and during machine operation, during which they can be subjected to both tensile and compressive stresses. Additionally, when laminated sheets are assembled to form cores in rotating machines and transformers, significant forces can be generated, as discussed in [17, 18]. For instance, in motors and generators, the combination of inertial forces and sharp geometries can result in the generation of highly intense local stresses [19, 20].

2.3.1 Press fit

Press fit is a widely employed joining technique in engineering, characterized by the insertion of one component into another by applying controlled pressure. This method is extensively utilized in various industries, including automotive, aerospace, electronics, and manufacturing [21]. It provides a strong and secure connection, simplifies the assembly process, and reduces costs. The absence of thermal stress during assembly minimizes the risk of material damage, making it suitable for delicate components [22]. However, achieving the optimal interference fit and considering factors like dimensional tolerances, surface finish, and material selection are crucial for successful press fit assembly.

2.3.2 Shrink fit

Shrink fit is also a technique in engineering for joining components by using the thermal expansion and contraction properties of materials. This method involves heating one component to increase its size and then fitting it onto another component

with a slightly smaller size. As the heated component cools down, it contracts, creating a tight and secure connection between the two parts [**?**]. Shrink fit assembly offers several advantages, including high strength, precise alignment, excellent torque transmission, and resistance to axial and radial loads.

2.3.3 Principal Stress

When identifying residual stress in a stator core material, the principal stress takes into account the magnitude and direction of the stress. Magnitudes of principal stress and their principal angle are calculated using [18]

$$\begin{aligned}\sigma_1 =& \sigma_\theta \cos^2\theta_\sigma + 2\tau_{r\theta}\cos\theta_\sigma \sin\theta_\sigma + \sigma_r \sin^2\theta_\sigma \\ \sigma_2 =& \sigma_\theta \sin^2\theta_\sigma - 2\tau_{r\theta}\cos\theta_\sigma \sin\theta_\sigma + \sigma_r \cos^2\theta_\sigma \\ \theta_\sigma =& \frac{1}{2}\tan^{-1}\frac{2\tau_{r\theta}}{\sigma_\theta - \sigma_r}\end{aligned} \tag{2.11}$$

where σ_θ and σ_r are stress components in the radial and angular directions respectively, σ_1 is maximum principal stress (tensile stress), σ_2 is minimum principal stress (compressive stress), θ_σ is the principal angle that produces the maximum or minimum stress and $\tau_{r\theta}$ is the shearing stress. Principal stresses are generated in the stator of motors when a stator housing is fitted to the stator through a joint fit.

2.4 Literature study

A literature study was conducted regarding the effects of stresses on electric steel sheets.

[23] measured the effect of compressive as well as tensile stresses on the magnetic properties of silicon steel sheets and found that stress has an impact on the magnetic properties of silicon steel sheets. They found that permeability of the material increased due to tensile stress up until 10 MPa. They also found that the permeability of the material decreased for all magnitudes of compressive stress tested. [24] investigated the variation trends of the comprehensive magnetic properties of silicon steel sheets under the combined influence of different stresses and excitations. It was found that the iron losses of grain-oriented silicon steel sheets were less affected by tensile stress at the same frequency, while they were more affected by compressive stress. Under the same compressive stress, an increase in frequency had a certain inhibiting effect on the increase of iron losses. When both frequency and compressive stress were simultaneously changed, the influence of compressive stress on the increase in iron losses became more significant.

[25, 26] utilized a stressing device to investigate the impact of mechanical stress on non-oriented Si-Fe steels in various cutting directions. The findings revealed that low magnitudes of tensile stress improved magnetization and permeability of the material, but at higher stress magnetization and permeability were reduced. The

tensile stress at which this change in behavior occur was shown to depend on the cutting angle. Compressive stress was found to reduce magnetization and permeability, regardless of cutting direction relative to the rolling direction. [27] found that the loss coefficient increase due to compressive stress was similar in the rolling and transverse directions, suggesting the possibility of developing a general formula for both cases. [28] observed the micro-structural variations in magnetic domains of electrical steel under tensile stress, to better understand the changes in magnetization due to tensile stress stress. [29] developed a testing device that is similar to the standard Single Sheet Tester (SST) and investigated the effects of compressive stress and tensile stress on the magnetization curves of grain-oriented Fe-3% Si steel. The conclusion drawn was that tensile stress compresses the hysteresis loop, while compressive stress elongates it. [8] conducted experiments by applying elastic tensile and compressive stress to non-oriented Fe-3% Si steel. It was observed that the hysteresis curve of the steel undergoes significant changes based on the magnitude of the applied stress. Tensile stress was found to facilitate the magnetization process up until 10 MPa, after which it deteriorates the magnetization process, while compressive stress deteriorated the material at all magnitudes of compressive stress, causing the hysteresis loops to become constricted. In a separate study, [30] conducted tests on silicon steel material under both tensile and compressive stresses using a device of their own design, and the test results showed that compressive stress had a larger impact, reducing material permeability and increasing losses.

The experimental results of previous works collectively point to a decrease in the magnetic induction strength of electric steel sheets when subjected to compressive stress. Hysteresis loops were elongated and permeability was reduced due to compressive stress, even at low stress magnitudes. In regards to tensile stress, previous works show that tensile stresses improve magnetic properties of electric steel at low amounts of stress, but has a negative impact on the magnetic properties at higher magnitudes of stress.

3

Develoment of Frame and Experimental Setup

3.1 Frame design

A custom magnetized frame was developed to closely resemble an SST with the possibility of applying compressive stress. In this section, the used frame design, as well as verification of the design, are presented along with the other equipment used when using the magnetizing frame to run tests.

3.1.1 Verification of frame design

Before construction, the proposed magnetizing frame was built in Ansys Maxwell where it was compared to a standard SST (as seen in Figure 3.1). For the simulations, ferrite, predefined in the system library, was used in the arms of the frames, while the material for the central lamination was created based on values from the data sheet of the material NO-25 1350H [31] that is studied in this thesis. This comparison was done in order to ensure that the developed frame functions were similar to those of an SST and that flux leakages in the corners on the right side of the frame are neglectable.

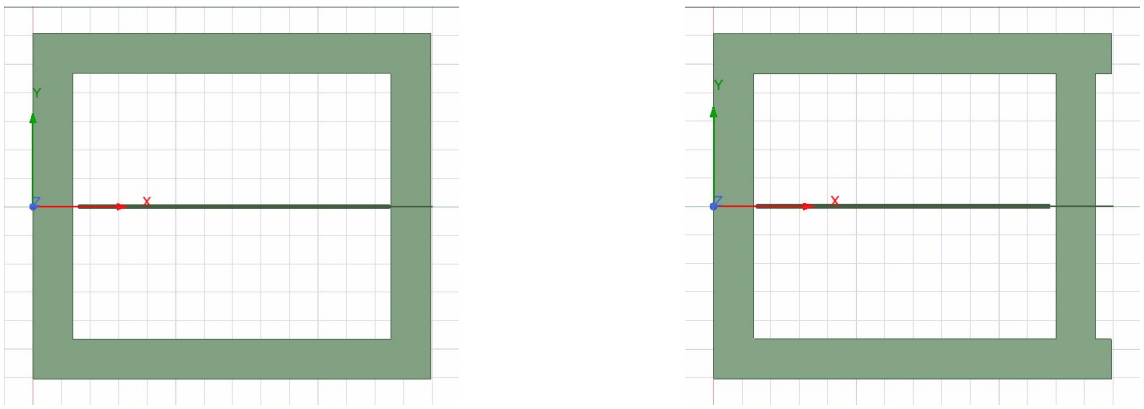

(a) Standard SST

(b) Custom frame

Figure 3.1: 2D Design of custom frame (b) as compared to a standard SST (a) in Ansys Maxwell at approximately 1.42 T excitation

An example comparison between the BH-loop measurements of the frames at approximately 1.42 Tesla excitation can be seen in Figure 3.2. Secondary voltage and primary current was extracted from the results of the transient study and (2.8) and (2.9) were used to determine H and B, respectively. As can be seen, the differences in design between the developed frame and the SST have little impact on the measured value. As such, effects of potential leakages due to the outreaching areas in the right corners can be neglected.

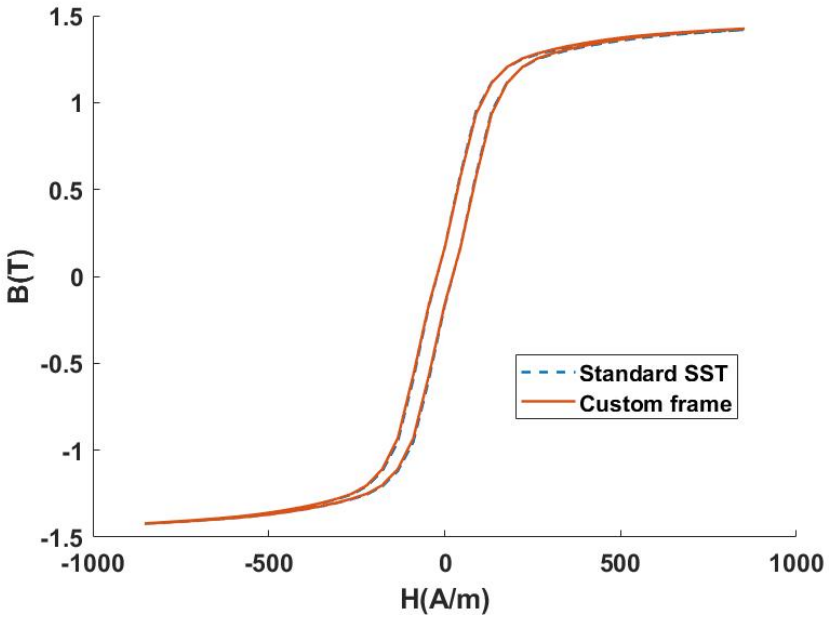

Figure 3.2: BH-loop of NO-25 1350H in Ansys Maxwell

3.1.2 3D design of frame

The Computer Aided Engineering (CAE) software, Solidworks®, was used to develop a 3D design of the custom frame to be constructed for this thesis. The design sketch is shown in Figure 3.3. The frame was modeled according to Figure 3.2 to closely resemble a horizontally lying SST.

The main body of the frame is a rectangle with four grooves along each of its sides to fit pieces of ferrite that are used to complete the magnetizing path. Several ferrite pieces are combined using tape to form two U-shaped ferrite cores. The test samples are vertically placed in the frame after being inserted into the coil, with the heads and tails of the U-shaped ferrite cores clamping the ends of the samples. The frame is secured with screws aimed towards the ferrite cores to press the ferrite cores toward the center of the frame. This reduces the air gap between the ferrite cores and surface of the samples surface, in order to prevent flux leakages and ensure that the flux path is not disturbed. Another advantage of this design is that the horizontal (90° shifted) force on the sample ensures that it will not bend or become damaged under compressive stress, leading to additional losses. A clamp is also placed at the

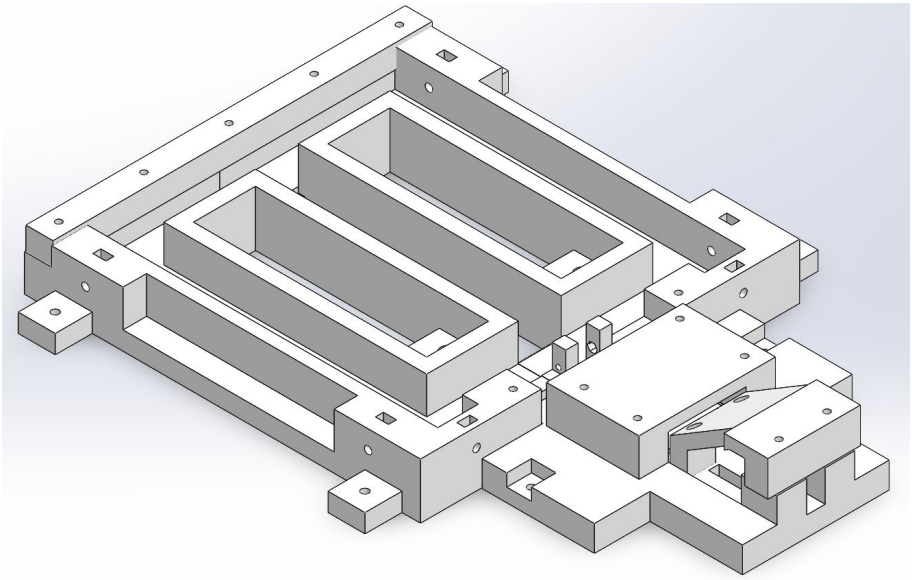

Figure 3.3: 3D design drawings

pressure application point of the samples to hold them in place and prevent bending after pressure application.

The other part that was developed for the frame is a platform on which the load cell and the pressure device are placed. The platform is connected to the main body of the frame with screws and consists of three parts: the platform bottom, the load cell cover, and the pressure device cover. The height of the platform bottom is identical to that of the main body of the frame, ensuring that the force from the pressure device is applied horizontally to the sample. Both the load cell and the pressure device are fixed on top of the platform using covers. They serve the purpose of wrapping and fixing the components completely to the base to prevent them from warping due to pressure during the pressurization process, resulting in inadequate or inaccurate force application.

Each component of the frame was 3D printed using $UltimakerExtendedS3$ and $UltimakerS5$ 3D printers. The plastic filament used for printing is ABS material, which possesses sufficient strength to withstand compressive stress exceeding 45 MPa. It is also more durable than many other plastics, which is ideal since the goal is for the frame to be used for future works as well. Detailed settings used for the 3D printer when printing the frame can be found in the Appendix A.1.

Due to the limitations of the 3D printer's size, the frame was divided into a total of six parts, as illustrated in Figure 3.4. The main body of the frame was separated into left and right parts, with an additional connecting piece used to reinforce the back end of the frame, as seen on the left side of the figure. The front of the frame, which can be seen on right side of the figure, consists of the platform that houses the load cell and pressure device, including the base and cover for the load cell and pressure device.

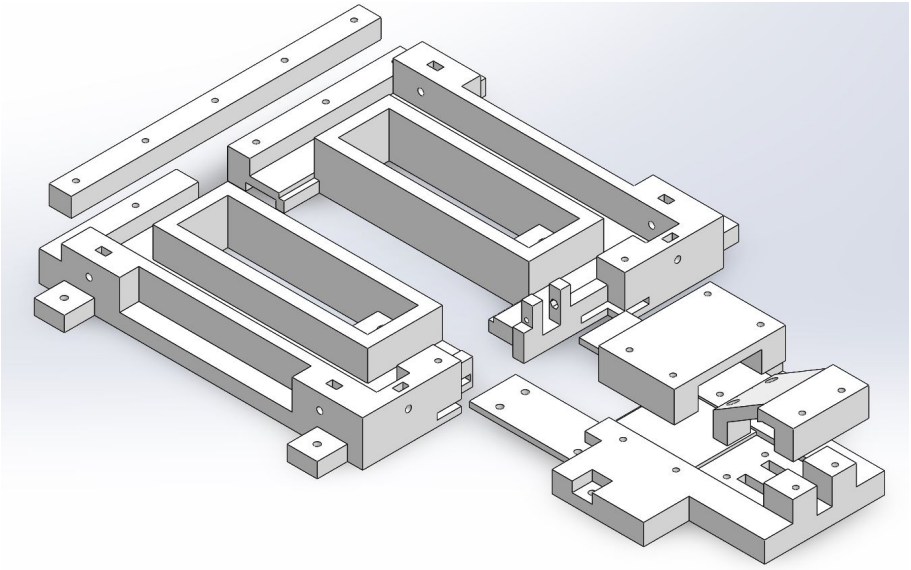

Figure 3.4: 3D model exploded view

3.2 Coil design

The coil was designed so that the frame would function at frequencies up to 1 KHz. In order to manage this, the equation

$$emf(rms) = 4.44BAfN_{turn} \tag{3.1}$$

was used, where emf is the voltage induced in the primary winding, A is the cross section area enclosed by the winding and N_{turn} is the number of turns of the primary winding.

The number of turns was chosen based on voltage rating of the power amplifier, number of samples needed in the coil, maximum excitation level to be achieved and the maximum target frequency. The value used are given in Table 3.1.

Table 3.1: Parameters used when designing the coil

Parameter	Symbol	Value
Voltage rating	V_{max}	100 [V]
Number of samples	N_{sample}	5
Thickness of sample	t_{sample}	0.25 [mm]
Width of sample	w_{sample}	30 [mm]
Number of primary turns	N_1	200
Number of secondary turns	N_2	100
Maximum flux density	$B_{p,max}$	1.8 [T]
Maximum frequency	f_{max}	1200 [Hz]

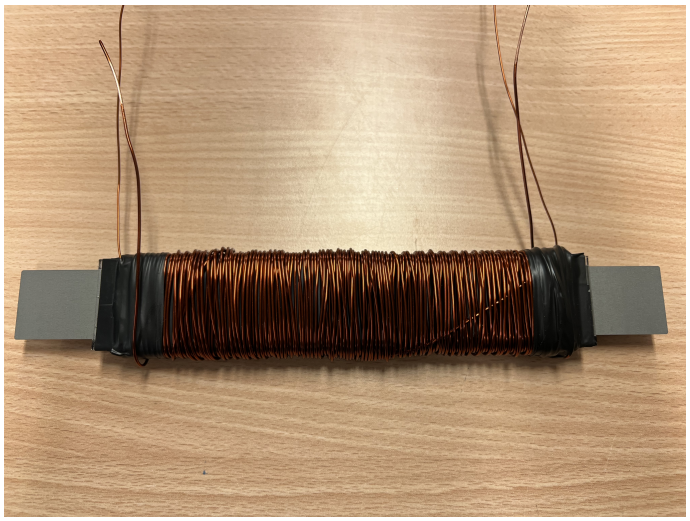

Figure 3.5: Coil developed for frame

3.3 Load cell

A load cell was utilized to determine the magnitude of compressive stress applied to the sample. The selection of load cell was made based on the required level of compressive stress for the experiment. Applied pressure is calculated using

$$P = \frac{9.80665m}{A} \tag{3.2}$$

where m is total mass of the applied force and A is the area that the force is applied to.

As seen in Table 3.2, in order to measure 70 MPa stress applied to 5 samples, the load cell needs a capacity of at least 287.68 kg. With this in consideration, the *RS Pro Alloy Steel S Beam Tension Load Cell* was opted for. The load cell is shown in Figure 3.6 and specifications are given in [32]

Table 3.2: Load cell capacity needed to measure 70 MPa

Number of samples	Maximum mass [kg]
1	53.54
2	107.07
3	160.61
4	214.14
5	267.68

It has a capacity of 300 kg with an output to input ratio limit of $2.0mV/V$. In the experimental setup, 10 VDC is sent to the input of the load cell using a SWITCHBOX 6303DS, and output voltage is measured using a multimeter KEYSIGHT U1272A (as shown in Figure 3.7). At 10 V input, the maximum output voltage is 20 mV. Dividing the maximum output voltage by the maximum range yields 0.0667 mV/kg,

Figure 3.6: Load cell

or 15 kg/mV. Thus, applied compressive stress can be measured by monitoring the values of multimeter.

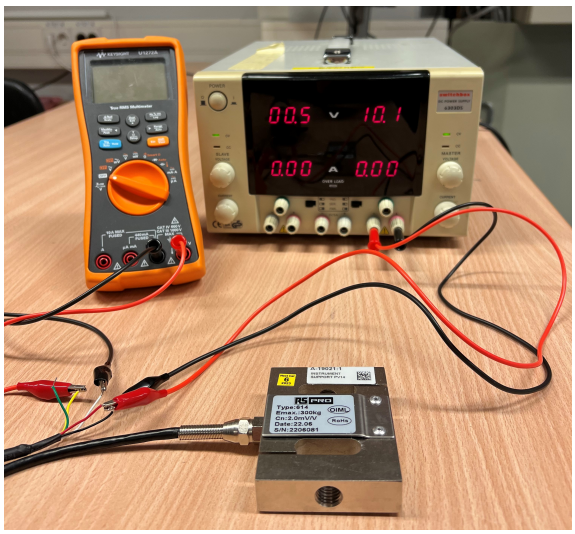

Figure 3.7: Load cell setup

3.4 Brockhaus equipment

The custom frame was connected to a Brockhaus Electrical Steel Tester $MPG-200$ shown in Figure 3.8 [33], specifically designed for determination of the magnetic properties of electrical steel and other soft magnetic materials, in compliance with the European standard IEC 60404 [15]. By connecting different sensors to the host computer, different soft magnetic material properties can be measured through the

use of the Epstein frame, SST, Stator tester, BST.

Figure 3.8: Brockhaus MPG-200

During the measuring process, electrical steel samples placed within a coil are subjected to a magnetic field, resulting in the generation of magnetic flux within the sheet steel. To supply the necessary electric current, a power amplifier is utilized. The current is then measured either by employing a temperature-stable, low-inductance precision resistor or through the use of field coils.

The determination of polarization is achieved through the sampling of the induced voltage, as well as conversion and integration of the voltage. For the parallel tracing of field strength and flux density separate analogue-digital converters are utilized to guarantee simultaneous measurements.

For this thesis, only Brockhaus' sinusoidal excitation is used to magnetize samples, although the Brockhaus equipment is capable of providing excitation through DC, square waves and Pulse Width Modulation, PWM, as well. Through the implementation of a control algorithm, the secondary voltage can be continuously monitored and regulated to align with the desired nominal value, where values for an entire cycle are measured. The frequency generator supplies the nominal voltage of selected frequency, with voltage being software-controlled depending on selected settings.

3.5 Assembly of the test setup

The assembled frame, as shown in Figure 3.10, is fixed onto an acrylic base using screws. The acrylic base (as seen in Figure 3.9) was laser cut from an 8 mm thick

acrylic sheet using a laser engraver of model $FusionM260WCO_2$ from Epilog Laser.

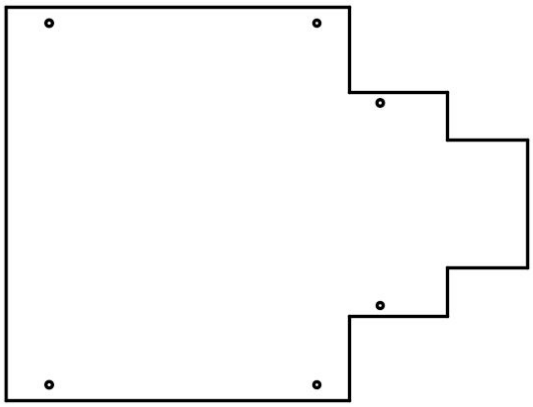

Figure 3.9: Acrylic base

The test samples are positioned within the coil in the center of the frame, with two U-shaped ferrite yokes screwed tight, clamping the samples. In order to ensure that multiple samples placed in the coil remain closely aligned without divergence or bending, steel clamps are used to clamp the end of the samples where pressure is applied. The load cell and the pressure device are arranged on the other side of the samples. The pressure device is a simple rotating mechanism, where pressure is applied by rotating a handle. These two devices and the coils are positioned at level height, ensuring that all compressive stress is applied in the horizontal direction onto the samples.

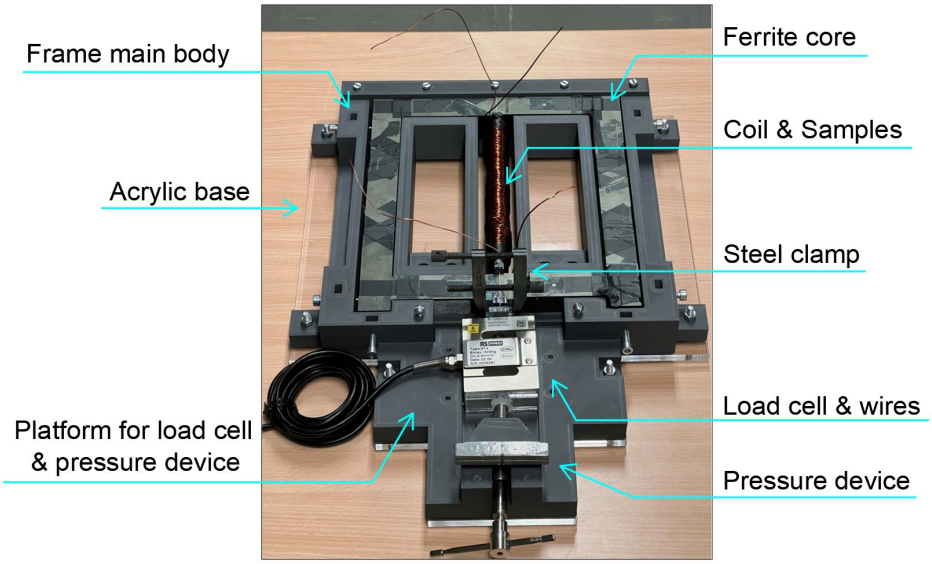

Figure 3.10: Frame

Once the customized frame, the pressure-displaying voltmeter, and the Brockhaus device are all connected, the schematic diagram of the entire experimental setup is

shown in Figure 3.11.

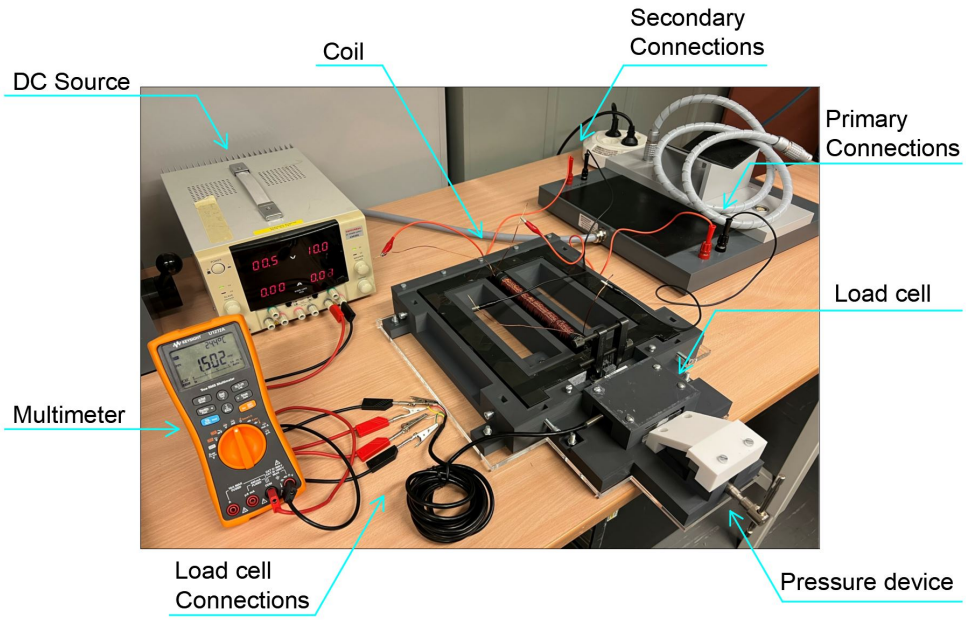

Figure 3.11: Frame setup

4

Custom Frame Tests Results

4.1 Validation of developed frame

The validation of the custom frame was assessed by comparing test results of the custom frame to the results of the standard Brockhaus SST and studying repeatability of the frame by repeating the same tests.

4.1.1 Verifying the reliability

Two laminations of NO-25 1350H electrical steel were inserted in the coil of the frame, and the primary winding (connected to Brockahus input) was excited with sinusoidal voltage at frequencies of 50, 200, 400, 700 and 1000 Hz. Field strength was measured using (2.8) and secondary voltage (connected to output of Brockhaus port) was measured to calculate flux density using (2.9). Excitation levels were selected as steps of 0.1 Tesla, ranging from 0.1 to 1.8 T for each frequency. For each excitation level, field strength and flux density were measured for an entire time period to trace the hysteresis loop of the material. In Figure 4.1 hysteresis loops at excitation levels of 0.1 to 1.4 T are shown.

The BH-loops measured using the custom frame were compared to BH-loops of the same material measured by the standard Brockhaus SST at different excitation levels (example comparison at 200 Hz can be seen in Figure 4.2). From the figures, it is clear that the values measured by the custom frame are very close to those measured by the SST for lower excitation levels. In (c) and (d) however, it is clear that the custom frame does not measure the same saturation point of the material as the SST does, since the field strength needed to reach those excitation levels in the SST is higher than in the custom frame.

In comparison to values from the data sheet [31] of the material, the Brockhaus SST measures saturation at lower excitation than what the data sheet shows, but this is most likely due to degradation of the material, since it has been laser cut into laminates. The custom frame showed an (almost) linear increase in H_{max} as function of excitation level, when the the excitation level is increased past 1.6 T, which indicates an inaccurate measure of the material saturation.

In Figure 4.3, the average relative permeability of the material measured by the custom frame and the SST for different excitation levels and frequencies is shown.

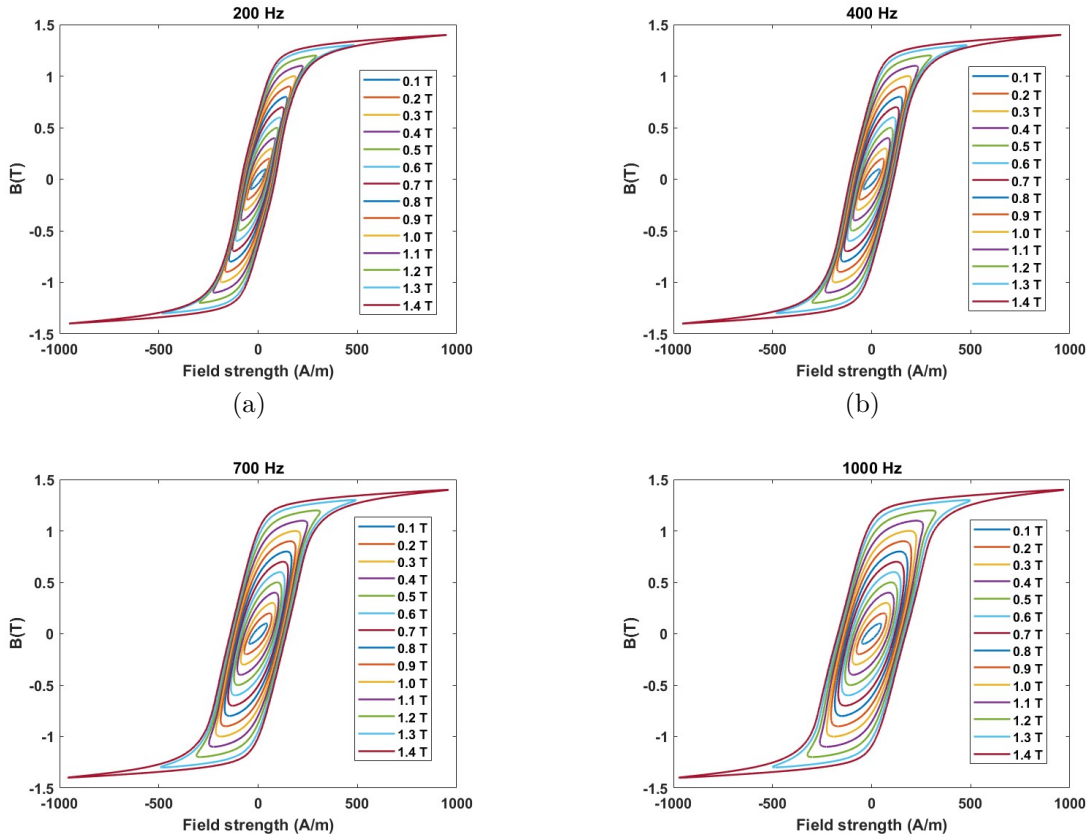

(a) (b) (c) (d)

Figure 4.1: Hysteresis loops at different excitation levels, measured by custom frame at (a) 200 Hz, (b) 400 Hz, (c) 700 Hz and (d) 1000 Hz

Average relative permeability of the material for a specific excitation level is calculated using

$$\mu_{r,average} = \frac{B_{max}}{H_{max}\mu_0} \tag{4.1}$$

where H_{max} is the peak measured field strength and μ_0 is permeability of vacuum. As can be seen, measured permeability is generally higher when measured using the custom frame than the SST. For high excitation levels, this is expected based on the results in Figure 4.2 since as the material saturates $\mu_r \to 1$ and the results from the SST show more of a material saturation than the custom frame does.

There are also differences in measured H_{max} at low excitation levels for operating frequencies of 400 Hz and 700 Hz. The custom frame measured higher average permeability here as well.

In Figure 4.4 it is clear that the measured losses in the custom frame are in good agreement with the losses measured in the SST. This is expected since losses are measured using (2.7), i.e. total losses are proportional to the area of the hysteresis loop. As seen in Figure 4.2, the hysteresis loops measured using the two frames have

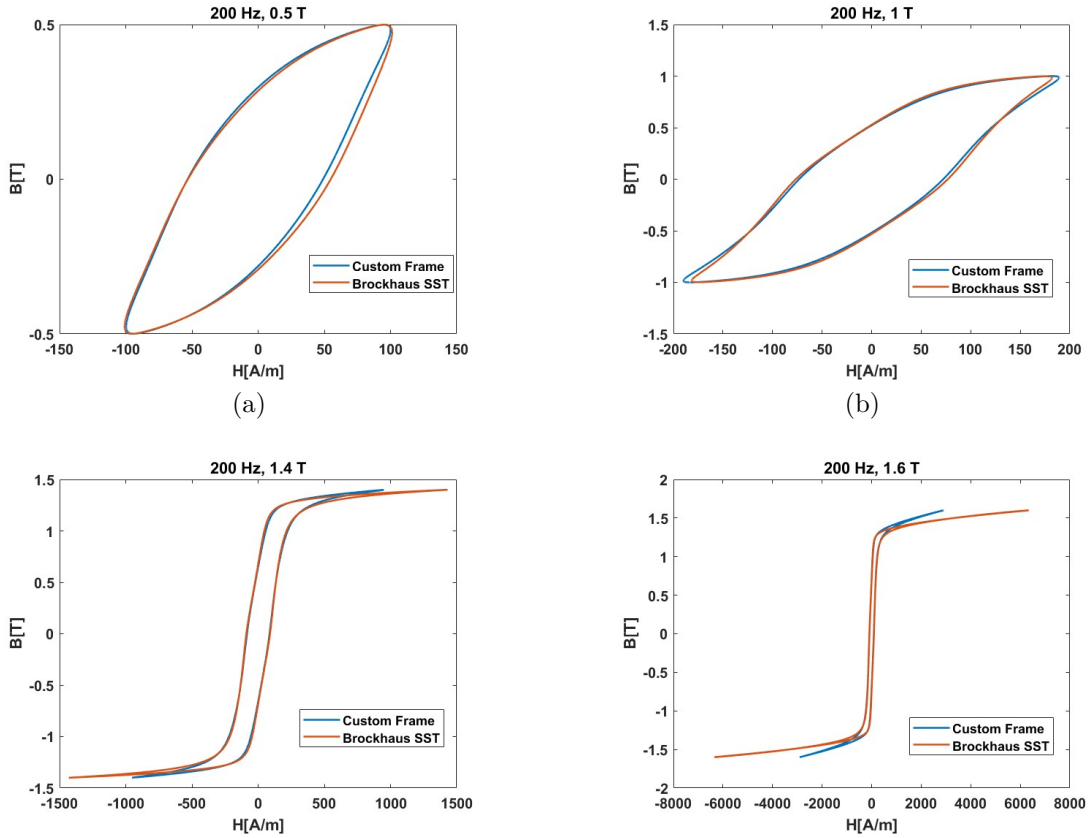

Figure 4.2: Comparison of measured hysteresis loops of material between custom frame and Brockhaus SST at (a) 0.5 T, (b) 1 T, (c) 1.4 T and (d) 1.6 T

similar shape and, thus, measured losses in the custom frame are close to the losses measured in the SST.

Overall, the developed custom frame shows good enough agreement with the Brockhaus equipment to be used for the purpose of this project. Losses and hysteresis loop shapes are in good agreement with the standard Brockhaus SST, while at higher excitation the frame does not measure the same level of material saturation. For the study of the effects of compressive stress on electrical steel, this is not a major problem however. Previous studies show a decrease in permeability at lower excitation levels as result of compressive stress, but at higher excitation levels (close to saturation) H_{max} is almost the same, regardless of the magnitude of compressive stress. Since the frame give reliable results of total losses and permeability at excitation levels below the saturation region, it will work for the purpose of this thesis.

4.1.2 Repeatability test

The custom frame was also tested for repeatability. An example repeatability test is shown in Figure 4.5, where the same test was conducted five separate times. The

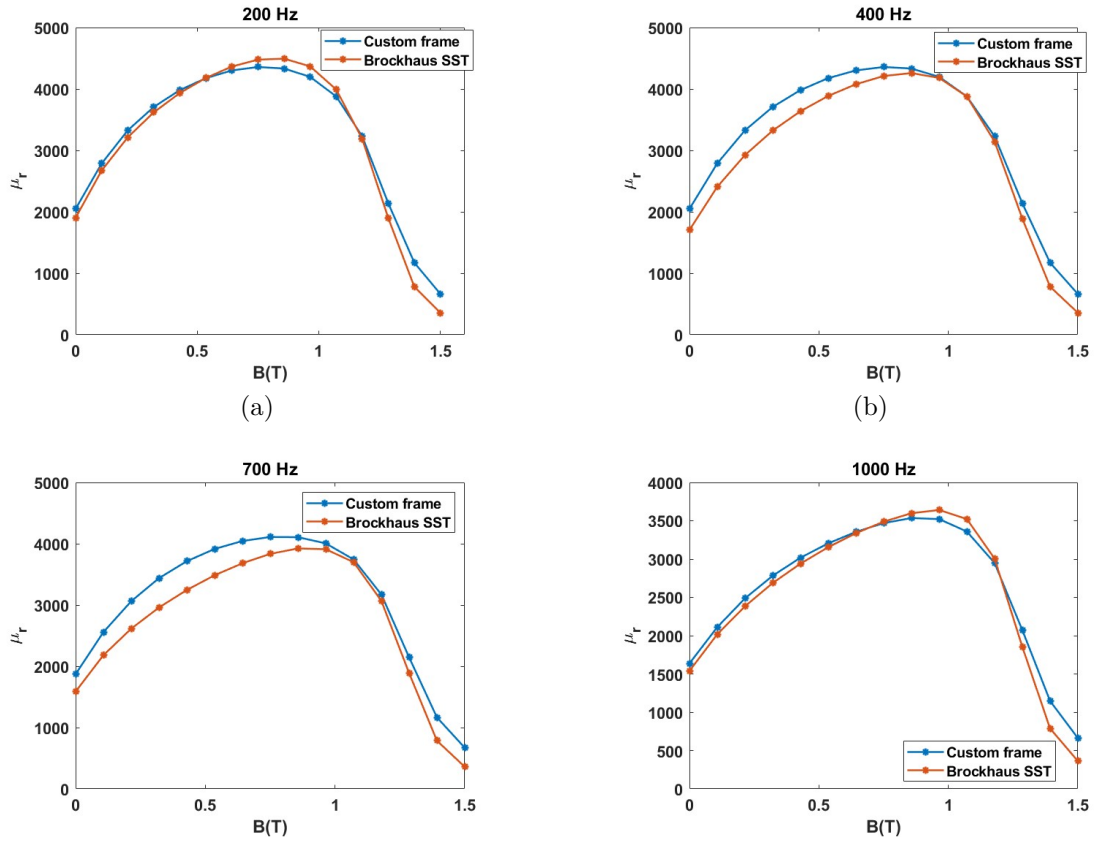

Figure 4.3: Comparison of measured relative permeability as function of excitation level between custom frame and Brockhaus SST at (a) 200 Hz, (b) 400 Hz, (c) 700 Hz and (d) 1000 Hz

results show that the measurements were consistent throughout the tests. There was a maximum deviation of 1.43% in measured losses between the tests, which is within the repeatability limits decided in the IEC Standards [15].

4.2 Compressive Stress Tests

In the experiment, compressive stress was applied up until a maximum of 60.6 MPa, in steps of approximately 5 MPa. The hysteresis loop of the material showed a significant change, as can be seen in Figure 4.7. It is clear that at 60.6 MPa of compressive stress, the B-H shape is deformed and the area of the loop has increased, leading to an increase in iron losses. In accordance with previous studies, in the saturation region (Figure 4.7(d)), the material under stress saturates at the same excitation level as in the case with no stress and H_{max} at excitation levels of 1.6 T and above show only a slight increase.

The average permeability of the material at $B_{max} \leq 1.5$ T has decreased due to

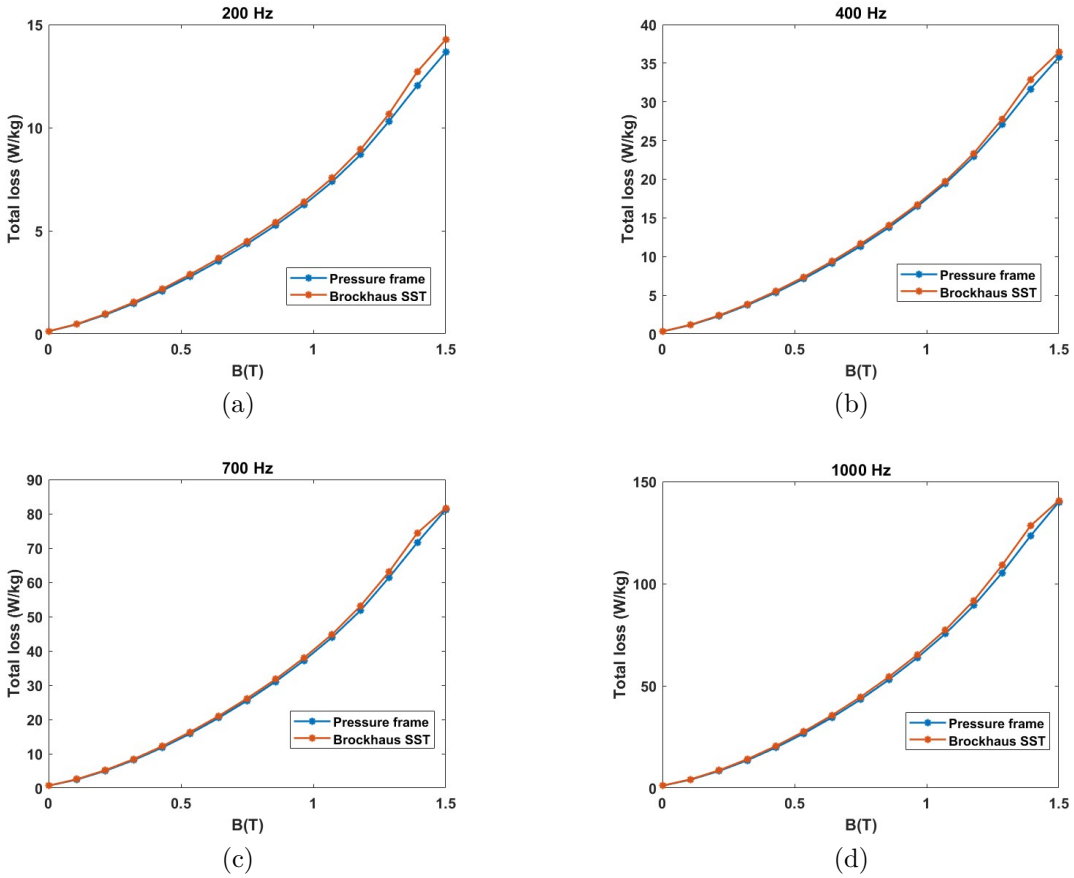

Figure 4.4: Comparison of measured total loss as function of excitation level between custom frame and Brockhaus SST at (a) 200 Hz, (b) 400 Hz, (c) 700 Hz and (d) 1000 Hz

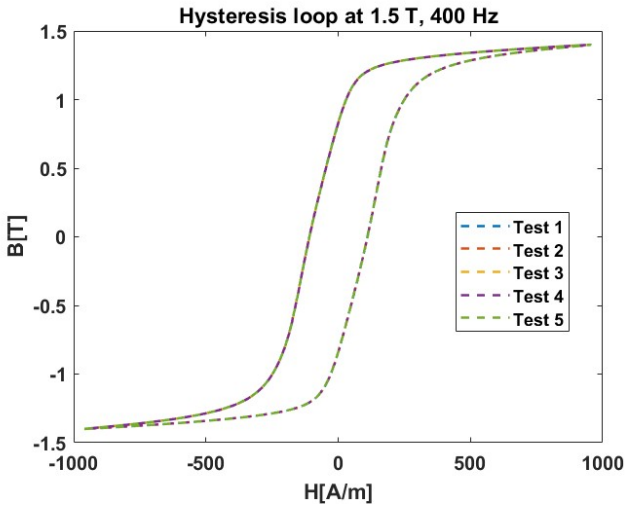

Figure 4.5: Hysteresis loop of material at 1.5 T excitation and 400 Hz frequency measured by custom frame in 5 separate tests

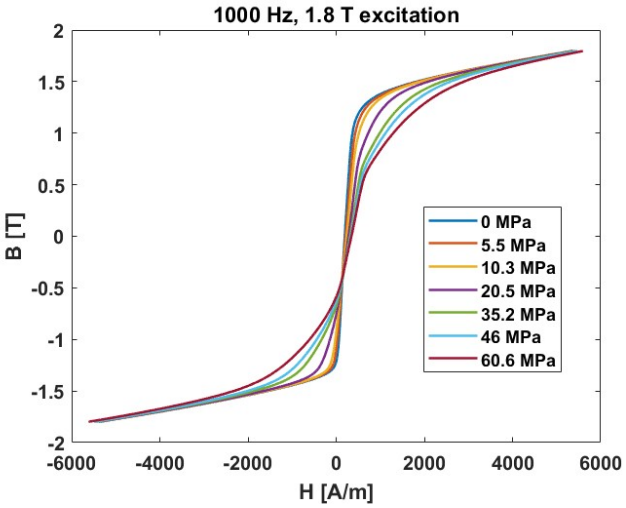

Figure 4.6: B-H curve of material as measured by custom frame at 1000 Hz and 1.8 T excitation when subjected to varying magnitude of compressive stress

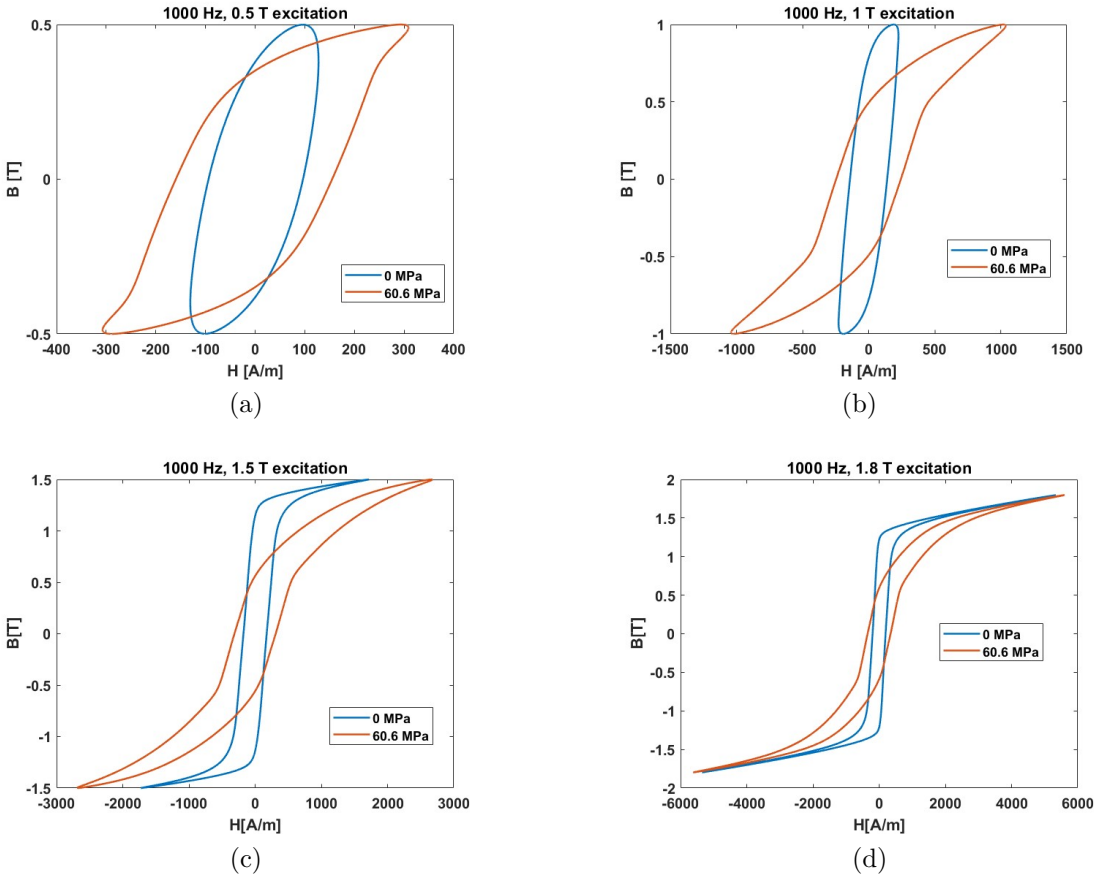

Figure 4.7: Hysteresis loop of material as measured by custom frame at no stress and maximum achieved compressive stress (60.6 MPa) at 1000 Hz and (a) 0.5 T, (b) 1 T, (c) 1.5 T and (d) 1.8 T excitation

the applied compressive stress (fig 4.8). Under no stress, relative permeability as function of B_{max} has similar shape to a second order polynomial function until the material saturates, with peak permeability at 0.8 - 0.9 Tesla, depending on frequency. Compressive stress decreases the peak permeability and at $-\sigma \geq 20.5$ MPa, the peak of the permeability curve is found below 0.5 Tesla excitation due to H_{max} increasing a lot with increasing B_{max} when compressive stress is applied. Even at low magnitude of compressive stress (-σ=5.5 MPa), average peak permeability of the material has decreased with 21 - 25.8 % for frequencies of 200 - 1000 Hz.

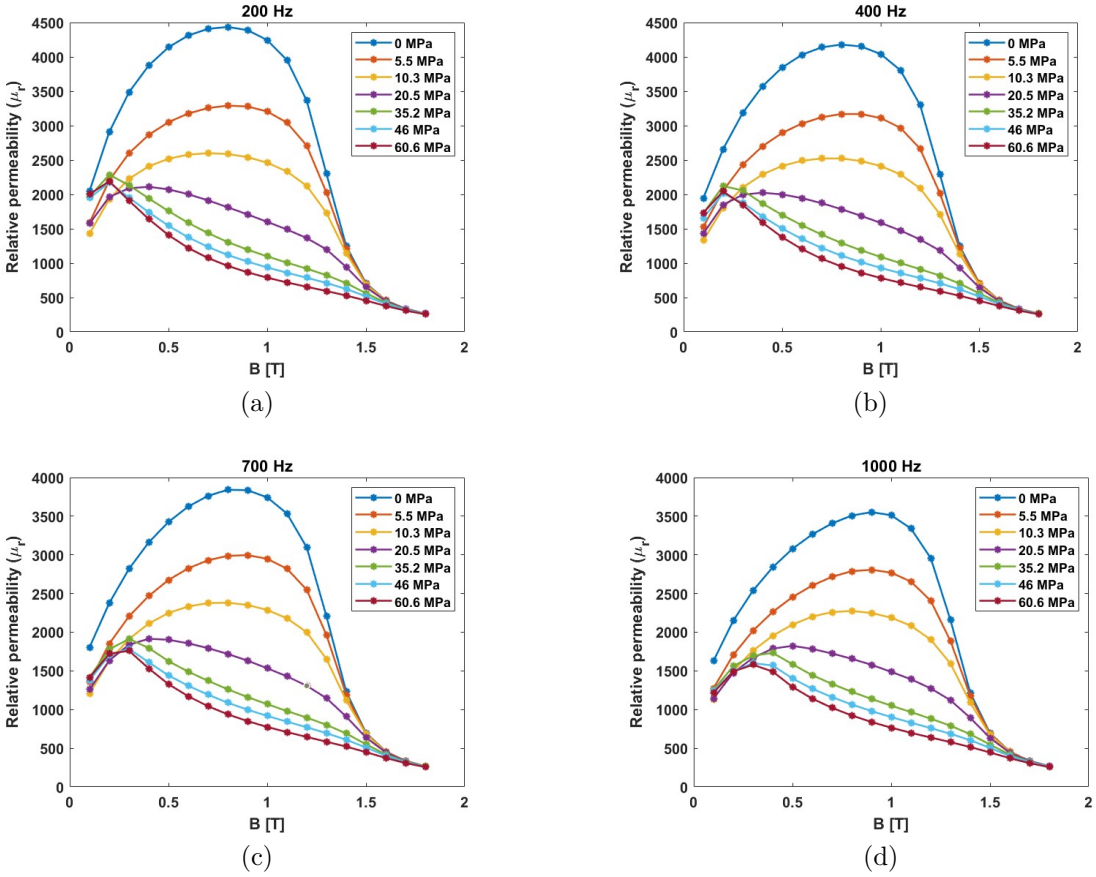

Figure 4.8: Relative permeability as function of excitation level for different magnitudes of compressive stress at (a) 200 Hz, (b) 400 Hz, (c) 700 Hz and (d) 1000 Hz

In Figure 4.9, permeability as function of compressive stress at 1 T excitation where permeability is near its peak (in the case of no stress) is studied. The change in permeability ($\Delta\mu_r(-\sigma, f)$) is high already at low compressive stress ($\Delta\mu_r$(-5.5 MPa, 200 Hz)= -1040). The results also shows that the effects of compressive stress on permeability of non-oriented electrical steels saturates as compressive stress continues increasing (in this case it starts saturating around 30 - 35 MPa).

In Figure 4.10 total measured losses per sample as function of excitation level for varying amounts of compressive stress are shown. The figures show an increase in total losses due to compressive stress, as expected based on the hysteresis loops seen

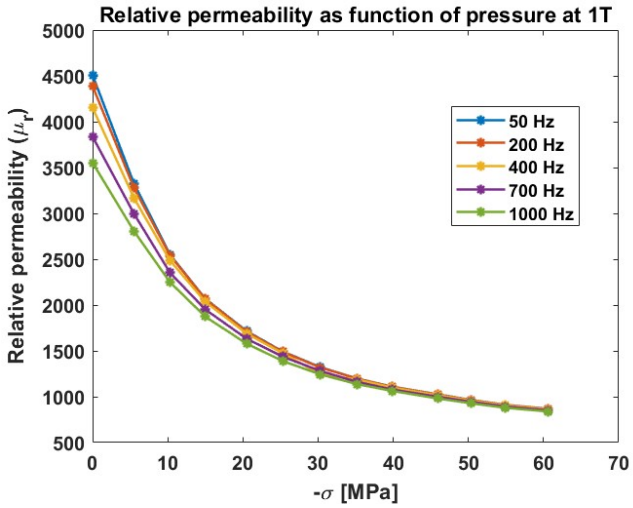

Figure 4.9: Average relative permeability at 1 Tesla excitation as function of compressive stress, as measured by custom frame for different frequencies

previously in Figure 4.7. If Figure 4.10(b) is used as an example, at 1.5 Tesla excitation and 400 Hz frequency, the loss is 36.65 W/kg without applied compressive stress, which increases to 43.32 W/kg at compressive stress of 10.3 MPa, showing a loss increase of 18.2%. At a compressive stress of 35.2 MPa, total loss in W/kg has increased by 45.9%, while at compressive stress of 60.6 MPa, it has increased by 49.11%, once again showing that the effects of compressive stress saturate when compressive stress exceeds 35.2 MPa. This is seen for all frequencies measured, indicating that the trend occurs for all frequencies within the frequency range. However, it can also be observed that the percentage increase in losses between 35.2 MPa and 60.6 MPa increases with frequency, indicating that the saturation is reduced as frequency increases. This indicates that high magnitudes of compressive stress has a larger impact at higher frequencies.

In Figure 4.11, total losses at 1.5 T are plotted as function of compressive stress. Both previous observations become more clear here, as losses become saturated when compressive stress increases, but the saturation is less at higher frequencies.

Total loss increase in % is given in Figure 4.12. An interesting observation is that at compressive stress of 20.5 MPa and higher, the loss percentage increase peaks at 0.8 - 0.9 Tesla for lower frequencies, while at 1000 Hz there is no such peak until the compressive stress is increased further (at 60.6 MPa). This indicates that the impact of compressive stress will vary a lot in a rotating machine depending on rotating speed and flux density in the machine. Overall, loss increase peaks at 74.88 % for a frequency of 1000 Hz, with applied compressive stress of 60.6 MPa, while loss increase is higher than 15 % at every excitation level, if the frequency is higher than 50 Hz and the applied stress is higher than 10.3 MPa.

Another interesting observation was made regarding the dependency of loss %-increase on frequency, excitation level and magnitude of compressive stress. The

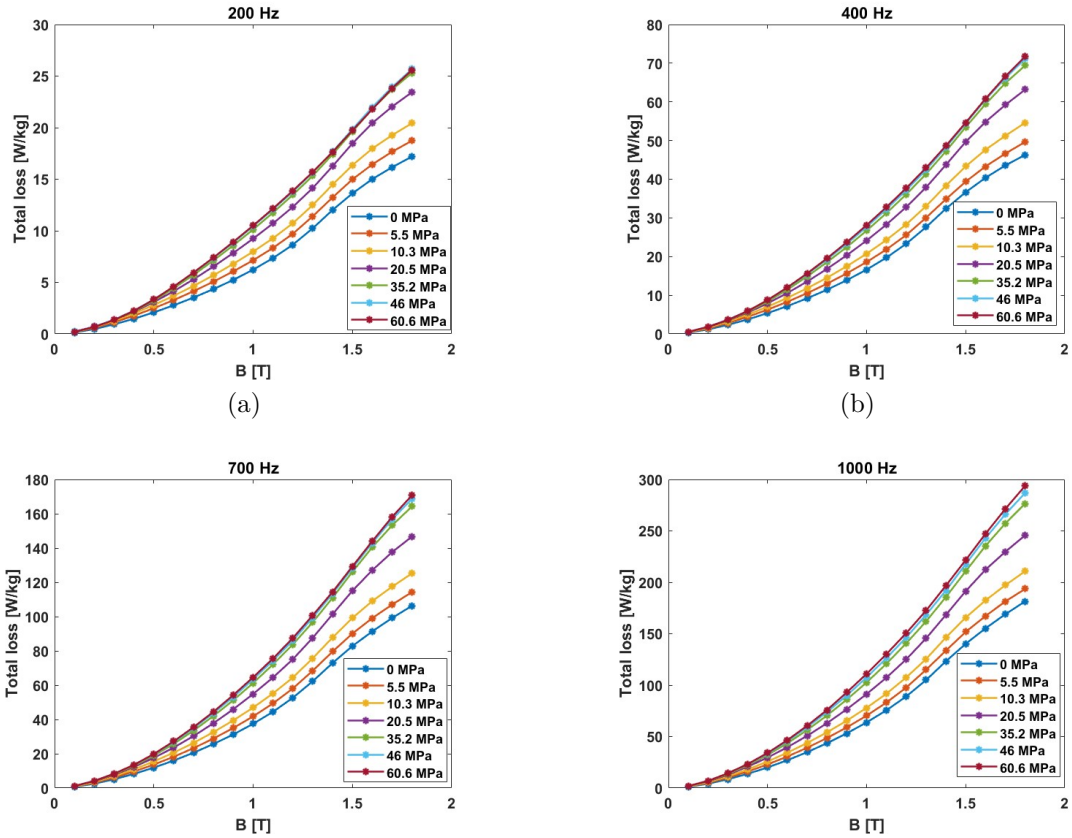

Figure 4.10: Total loss as function of excitation level for different magnitudes of compressive stress at (a) 200 Hz, (b) 400 Hz, (c) 700 Hz and (d) 1000 Hz

results indicate that at low stress, impact of stress is higher for lower frequencies, but at high stress the opposite occurs.

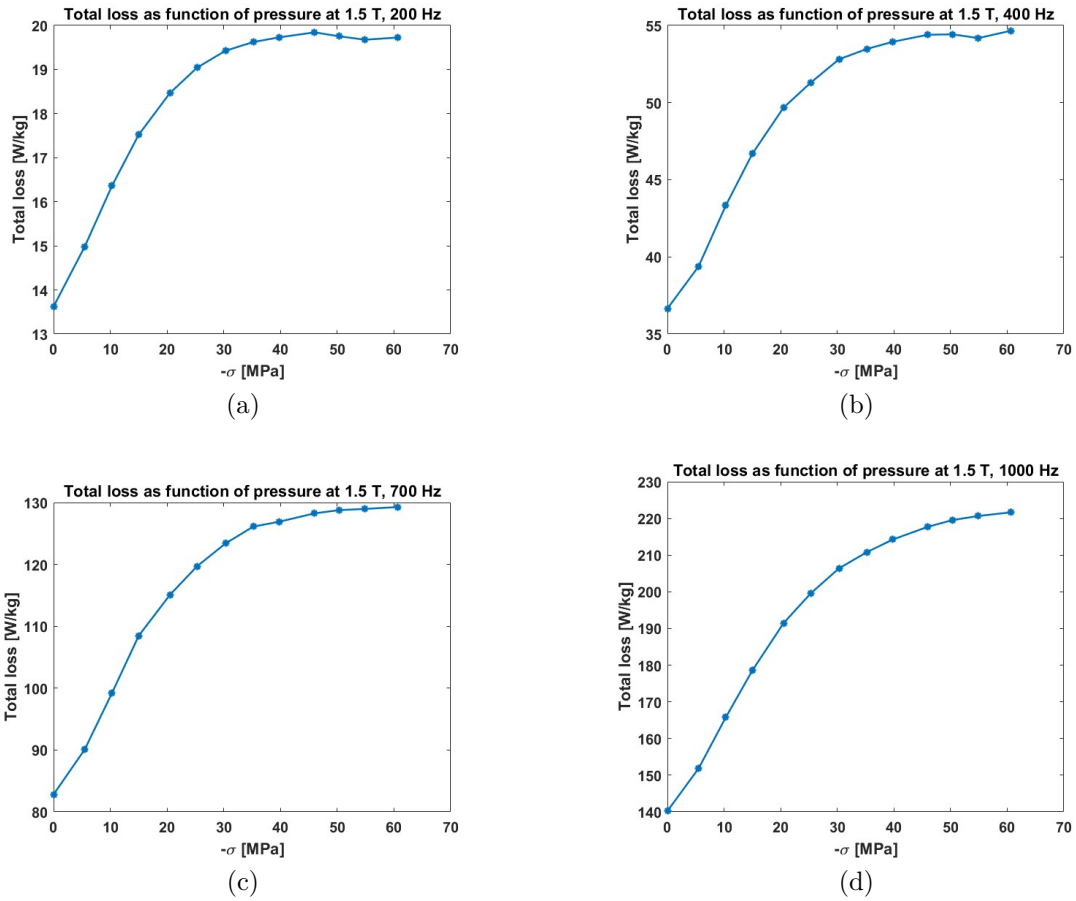

Figure 4.11: Total loss as function of compressive stress at 1.5 T at frequency of (a) 200 Hz, (b) 400 Hz, (c) 700 Hz and (d) 1000 Hz, as measured by custom frame

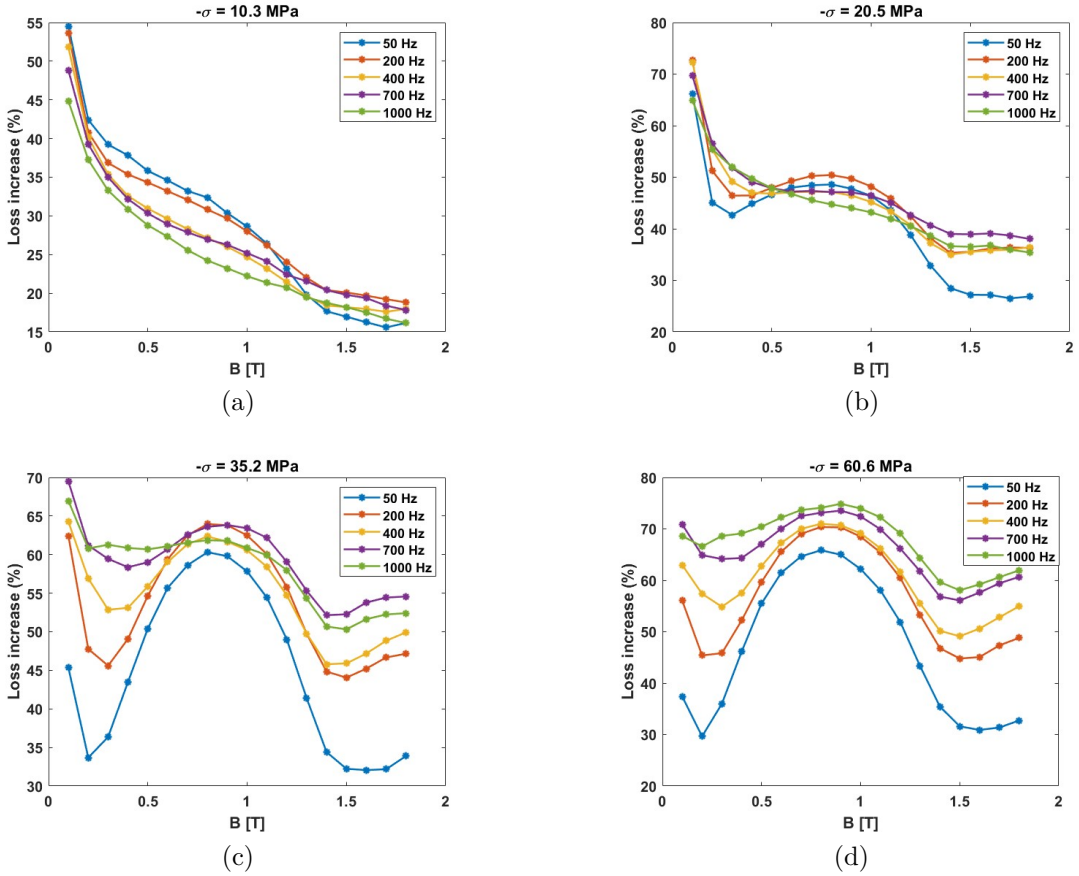

Figure 4.12: Total loss % increase at -σ = (a) 10.3 MPa, (b) 20.5 MPa, (c) 35.2 MPa and (d) 60.6 MPa

5

Effects of Stresses on Machine Performance in FEM-based Software

5.1 IPM design with stator housing

In order to analyse the effects of compressive stresses on the performance of a sample electric motor used in an electric vehicle, an 8-pole, 48 slot, V-shaped interior permanent magnet motor (IPM), was designed for finite element method, FEM, analysis in JMAG®. The parameters of the machine were selected to reach typical rating values of an electric motor. The electrical parameters of the designed motor are given in Table 5.1. Geometrical dimensions of the IPM are provided in Table 5.2. An aluminum stator housing, or stator frame, was also added to the design in order to simulate the effects of compressive stresses in the stator caused by the joint fit between stator and housing.

Table 5.1: Electrical Ratings for the PMSM

Parameters	Values
DC voltage	400 [V]
Maximum Output Power	220 [kW]
Maximum Torque	462 [Nm]
Maximum Speed	14000 [rpm]
Maximum Current	919 [A]

The finalised IPM with housing is shown in Figure 5.1. The yellow frame around the stator is the stator housing.

The Press Fit and Temperature Load conditions available in JMAG were used to generate stress distribution in the stator for two cases. In a real, 3-dimensional motor, the stress varies in the axial direction from the drive end of the motor to the other end. In the mid radial position of the stator, the compressive stress varies between approximately 15 and 35 MPa, depending on the axial position. Therefore one case with lower compressive stress and one case with higher compressive stress were studied. In the first case (Case A), generating lower stress, the stator housing is press fitted to the stator with an interference of 0.143 mm and in the other case (Case B) the same press fit is used, but a temperature load of -35 °C is also

Table 5.2: Geometrical dimensions of the PMSM

Dimensions	Values
Stator Diameter	235 [mm]
Stator Housing Thickness	3.5 [mm]
Rotor Diameter	148.72 [mm]
Active Length	125 [mm]
Shaft Diameter	58.32 [mm]
Number of Slots	48
Number of poles	8
Stator slot height	25.82 [mm]
Winding Type	Stranded
Number of Turns	5
Steel Material	NO25-1350H
Winding Material	Copper
Magnet Material	N42UH
Airgap	1[mm]
Magnet Pole Angle	150°
Magnet Thickness	5.92 [mm]
Magnet Width	21.11 [mm]

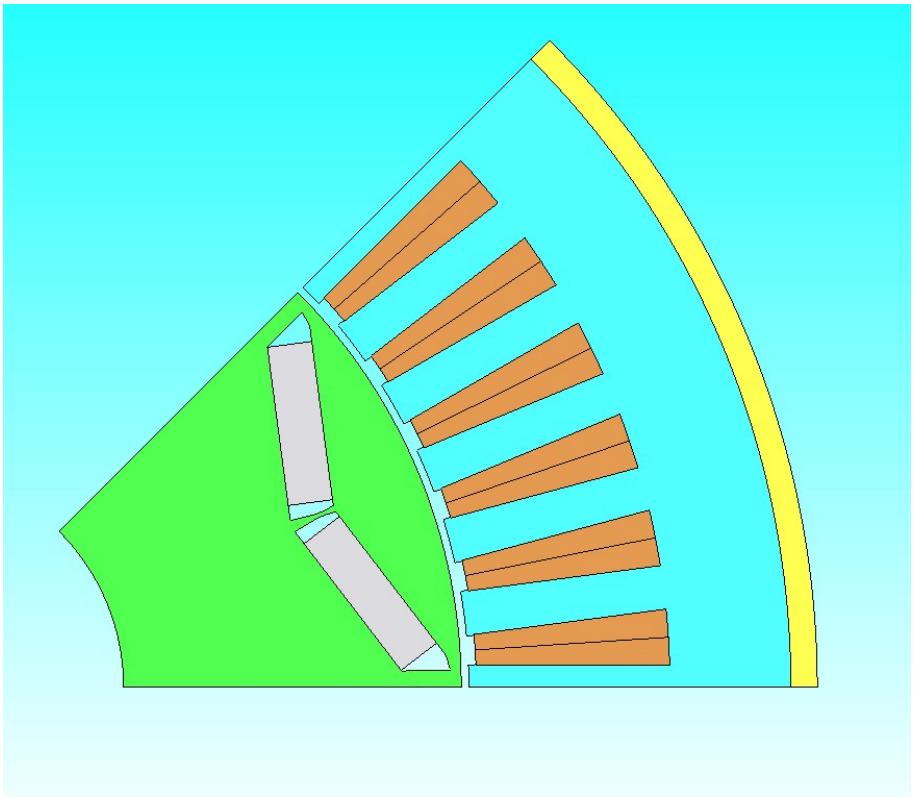

Figure 5.1: JMAG model of one pole of IPM

placed on the stator housing for thermal shrinkage of the stator housing to generate a higher stress. The values used for the stator housing material are given in Table 5.3.

Table 5.3: Material properties of stator housing

Property	Value
Thermal expansion	$2.07 \cdot 10^{-5}$/°C
Reference temperature	20 °C
Young's modulus	70 GPa
Density	2860 kg/dm^3

The minimum principal stress distribution, σ_2, in the stator for both cases can be seen in Figure 5.2.

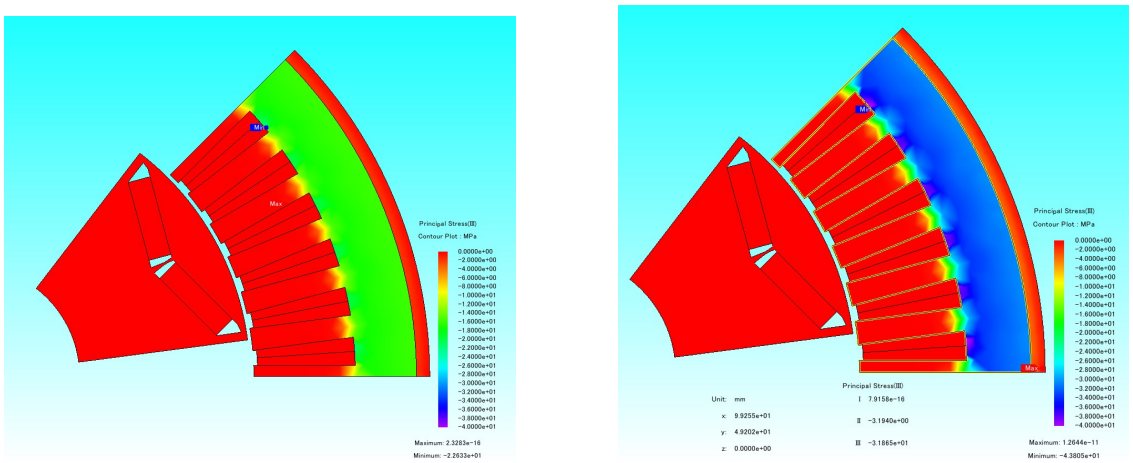

(a) (b)

Figure 5.2: Principal stress distribution (σ_2) in stator due to joint fit between stator and stator housing for (a) Case A and (b) Case B

In Case A, the compressive stress in most of the stator yoke ranges between 16 - 17 MPa. It increases to approximately 23 MPa close to the inner edges of the stator yoke close to the slots and there is no compressive stress in most of the stator teeth. This is due to the frame compressing in the radial direction and, while the compression is damped towards the tips of the teeth, the compression concentrates close to the slots due to lack of damping [34]. Thus, the interference fit is mostly impacting the iron losses in the stator yoke. In Case B, the compressive stress in most of the yoke ranges between 30 and 31 MPa. The compressive stress close to the slots peaks at 40 MPa.

The values obtained from the compressive tests were used to create NO-25 1350H in JMAG with B-H curves with compressive stress dependency and losses with compressive stress and frequency dependency. Due to the material not saturating completely at higher excitations, measured field strength values above 1.6 Tesla from the previous tests could not be used in the simulations. When those values were used, flux density in the stator was unreasonably high (since measured H_{max} in the custom frame at high excitation was too low), and iron losses, even without press

fit, would be too high. Therefore, values from 0.1 to 1.6 T were used and extrapolated using Multiphysics Comsol's B-H Curve Checker application where material saturation is taken into consideration to get H-values for higher excitation levels [35]. This was only done for the case with no compressive stress however, because the extrapolation becomes inaccurate when compressive stress is applied, due to the changes in B-H values. Since previous studies, as well as the results in section 4.2, show that compressive stress has only a slight effect on the saturation of the material, H_{max} at excitations above 1.6 T was assumed to be the same for all magnitudes of compressive stress. The B-H curves added to JMAG are shown in Figure 5.3. The material was used both in the rotor and stator.

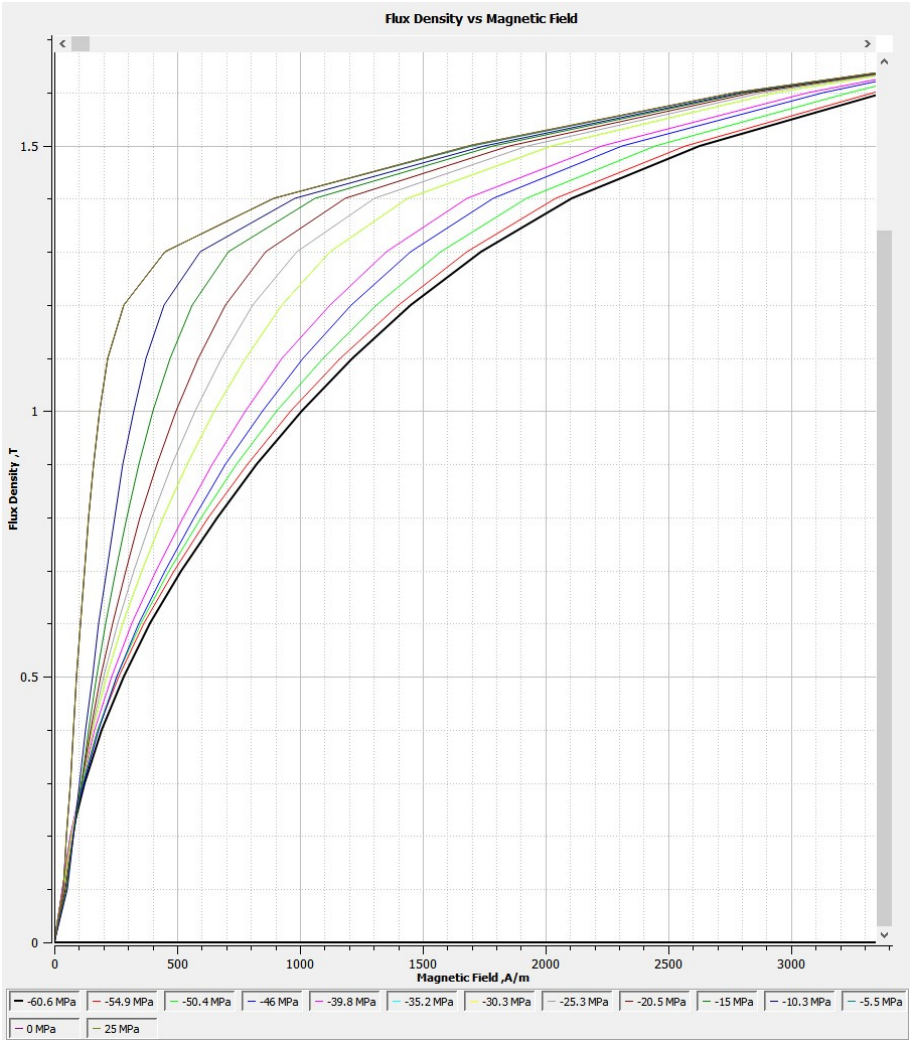

Figure 5.3: BH-curves of NO-25 1350H with dependency on compressive stress as added in Jmag

Electrical steel values for resistivity, density and Young's modulus were added based on values obtained in the data sheet of the material [31]. Measured total loss values from the compressive stress tests shown in section 4.2 were added to the material's database as frequency and stress dependent, as seen in Figure 5.4.

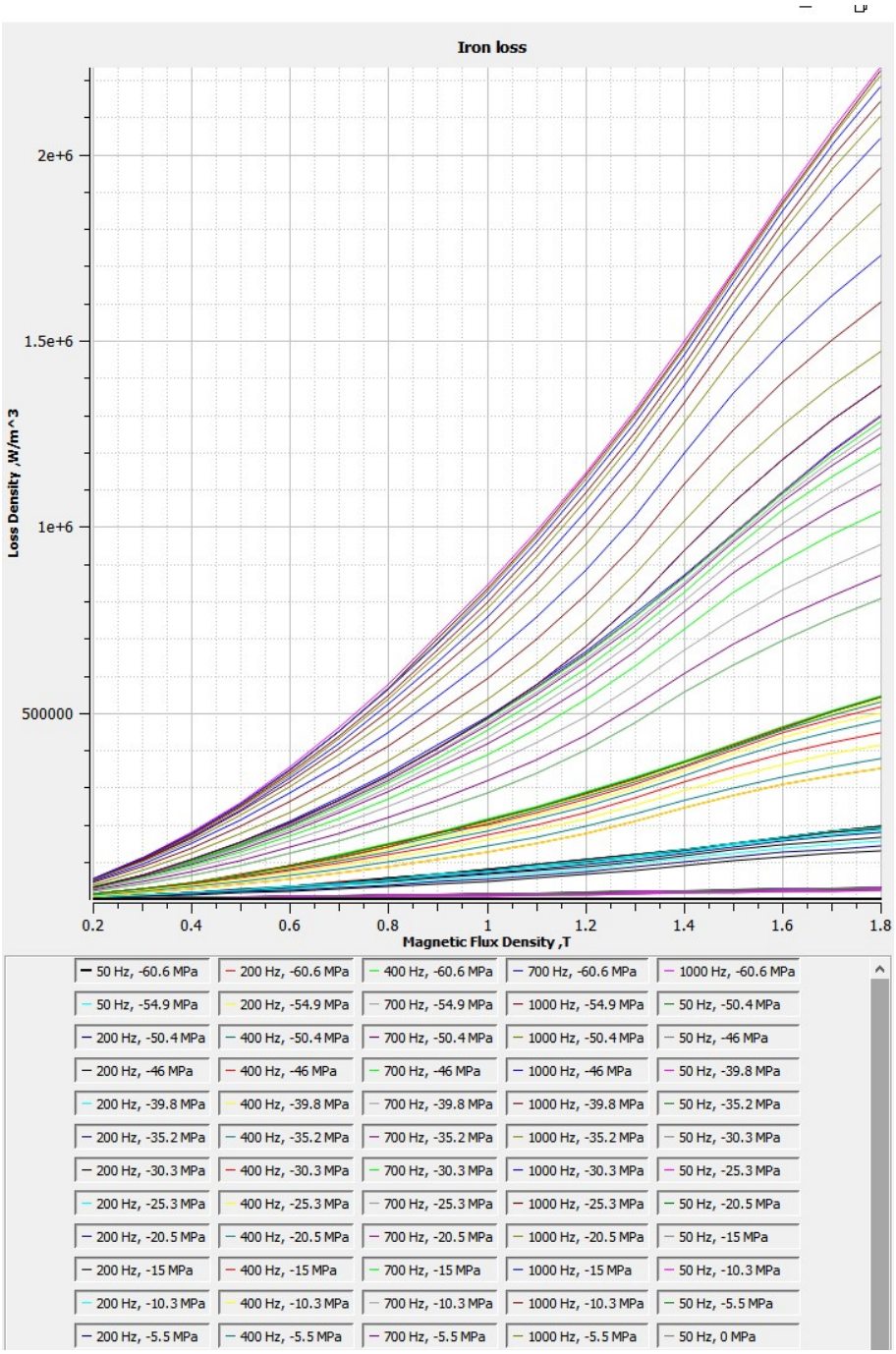

Figure 5.4: Loss curves of NO-25 1350H with dependency on compressive stress and frequency, as added in Jmag

5.2 Effects of joint fit on iron losses and machine efficiency

A speed priority of the IPM was executed, generating the motor's efficiency map (without stress distribution), as seen in Figure 5.5. The motor reaches field weakening at around 4000 RPM, its peak torque is 462 Nm and the efficiency in the operation range is reasonable. While the entire operation range is mapped, certain operation points of specific interest are also studied individually. These operation points are at speeds of 80 km/h and 120 km/h, which approximately correspond to a rotor speed of 5721 RPM with 20 Nm torque and a rotor speed of 8731 RPM with 30 Nm torque, respectively, for a smaller vehicle. These are crucial operation points, as these are common speeds in the drive cycles of vehicles. Later on, the efficiency of a drive cycle will also be studied and the parameters of the example vehicle used for that drive cycle are given in Table 5.4.

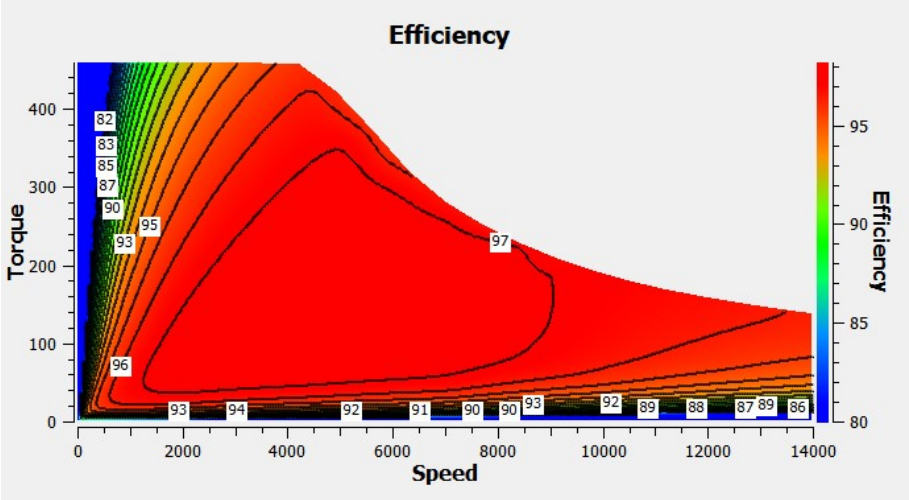

Figure 5.5: Efficiency map of IPM, generated in Jmag

Table 5.4: Parameters of example vehicle

Parameters	Abbreviation	Value
Mass	m	2000 [kg]
Rolling Resistance Coefficient	C_r	0.009
Frontal area	A	2.45 [m^2]
Gear ratio	k_{gear}	9.5
Wheel radius	r_{wheel}	0.35 [m]
Air drag coefficient	C_d	0.24
Gearbox efficiency	η_{gear}	1

Flux density variations at the previously mentioned operation points are presented in Figure 5.6. In 5.6(b), flux in the stator yoke is generally lower than in (a), which affects losses, but also affects the stress dependency of the stator losses, since the

dependency varies with flux density level as seen in Section 4.2.

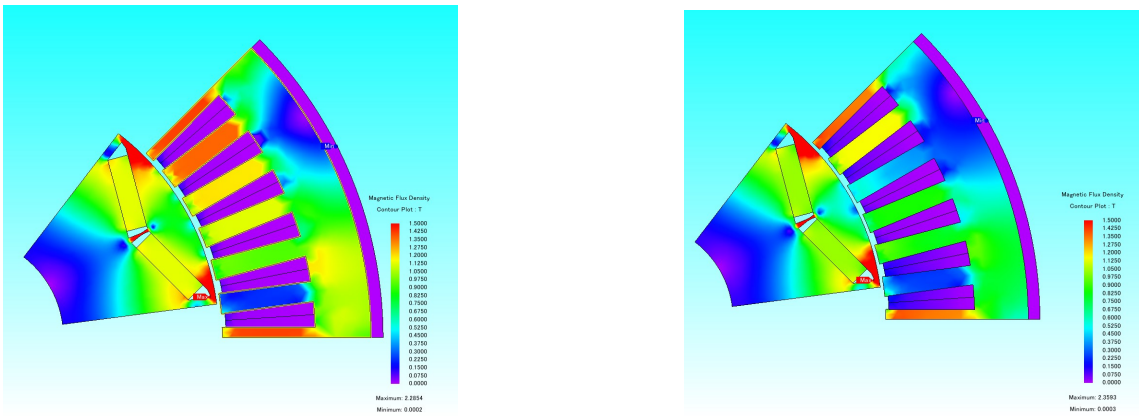

(a) ω_r = 5721 RPM, T = 20 Nm (b) ω_r = 8731 RPM, T = 30 Nm

Figure 5.6: Flux density in machine at operation point corresponding to (a) 80 km/h and (b) 120 km/h

In Figure 5.7, the iron loss density in the machine is shown at an operation speed of 5721 RPM with torque of 20 Nm. As expected, the impact of the joint fit is seen in the stator yoke, while the teeth are mostly unaffected. For the case with no stress, loss density in the stator yoke ranges from approximately 140 000 W/m^3 (at the outer edge of the stator) to 400 000 W/m^3 (at the tip of the teeth). For the same operation point, in Case A loss density ranges approximately from 180 000 W/m^3 to 435 000 W/m^3 and in Case B loss density ranges approximately from 195 000 W/m^3 to 450 000 W/m^3, showing a significant increase in loss density in the stator yoke due to the joint fit.

At the operation point corresponding to 120 km/h, without any stress, the loss density in the stator yoke varies between approximately 150 000 W/m^3 and roughly 700 000 W/m^3 (Figure 5.8 (a)). At the same operation point, for Case A the loss density in the stator yoke varies approximately between 205 000 W/m^3 and 750 000 W/m^3, while for Case B the loss density in the stator yoke varies approximately between 230 000 W/m^3 and 800 000 W/m^3.

The loss increase in the stator yoke is shown alongside total iron loss (rotor and stator) and total loss increase in Figure 5.8 for Case A as compared to the case with no stress. As previously observed in Figures 5.7 and 5.8, most of the loss increase due to joint fit occurs in the stator yoke. Loss increase in the stator yoke at torques lower than 150 Nm is approximately 19.7 - 25.5 %. The loss increase in the stator yoke is higher than 11.14 % in the entire operation range.

Total iron loss increase peaks at 10.53%. The % increase of total iron losses is considerably less than in the stator yoke, due to the steel in the rotor and most of the stator teeth not experiencing any stress. Here it can also be observed that % increase is less at higher speeds. Since loss increase in the yoke was high at all speeds,

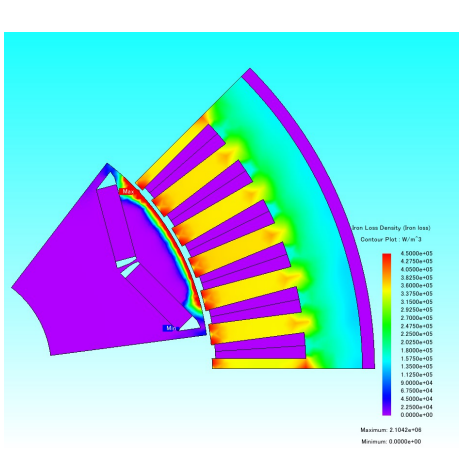

(a) No Stress

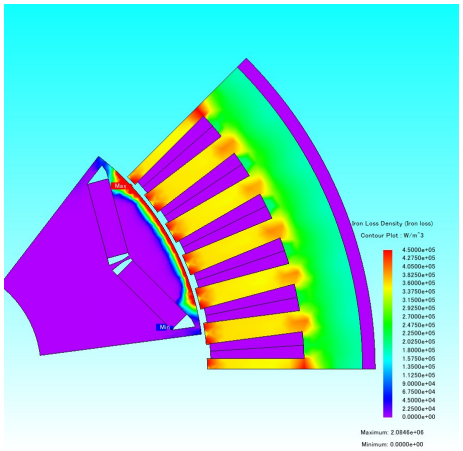

(b) Case A

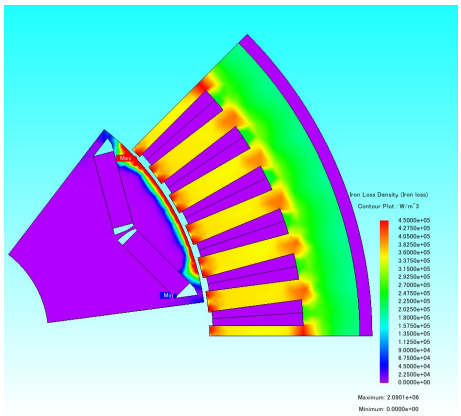

(c) Case B

Figure 5.7: Iron loss density in machine at 80 km/h for (a) no stress, (b) Case A and (c) Case B

this indicates that at higher speeds most of the iron losses are in the stator teeth and the rotor due to higher flux density. The % total loss increase in the machine ranges between 0.04 % and 9.76 % and it is higher at low speed and low torque. The reason for this is that copper losses are lower at lower torque.

In regards to the joint fit's effect on total efficiency of the machine, this is presented in Figure 5.10. The maximum efficiency decrease in the operation range of the machine is 0.74%, and the figure shows that the efficiency decrease is higher at low torque. At the operation points of specific interest, 80 km/h and 120 km/h, the efficiency decrease is approximately 0.42 % and 0.27 %, respectively, as seen in Figure 5.10(b). This shows that there is a considerable impact of a joint fit at lower torque.

For Case B, loss increases are shown in Figure 5.11. Loss increase is higher than in Case A, since more stress is generated by the housing. Loss increase in the stator yoke ranges between 17.05% and 39.77 % in the operation range.

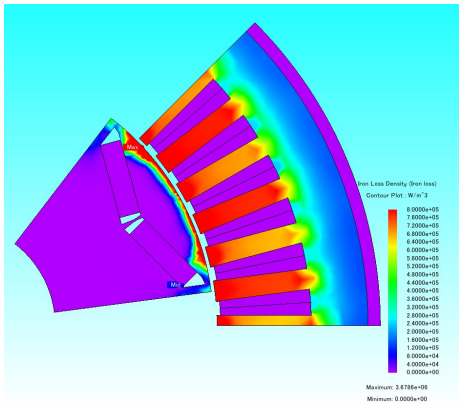

(a) No Stress

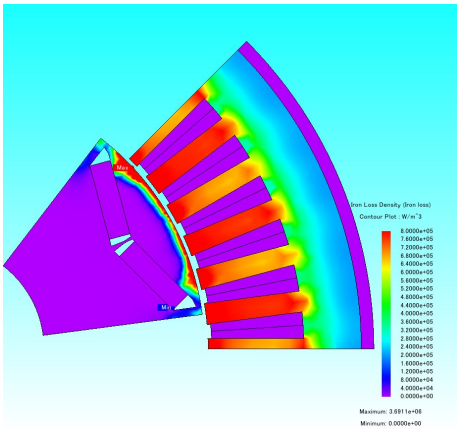

(b) Case A

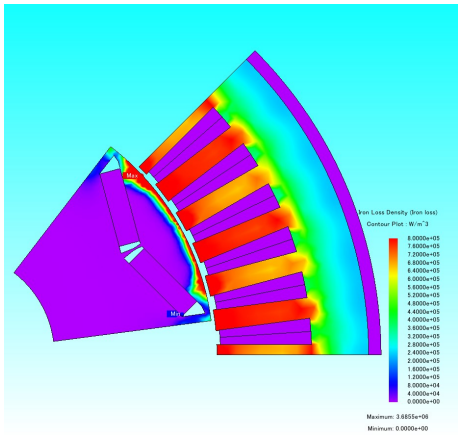

(c) Case B

Figure 5.8: Iron loss density in machine at 120 km/h for (a) no stress, (b) Case A and (c) Case B

The total iron loss increase ranges between 5.96% and 15.50 % and the total loss increase ranges between approximately 0.06 % and 15.16 %. The highest efficiency decrease in the operation range of the motor is 1.27 % (seen in Figure 5.12). At 80 km/h and 120 km/h, efficiency has decreased with approximately 0.65 % and 0.41 %, respectively.

The effects of the joint fit was also studied for a drive cycle. The drive cycle used for the tests is the Worldwide Harmonised Light Vehicle Test Procedure Class 3 cycle (WLTC-3) and it is shown in Figure 5.13. Corresponding rotor speed and torque at each point of the drive cycle for the example vehicle presented in Table 5.4 was calculated by using Newton's second law of motion and the following equations

$$F_{wheel} = \frac{1}{2}\rho_{air} C_d A v^2 + C_r mgcos(\alpha) + mgsin(\alpha) + m\frac{dv}{dt} \tag{5.1}$$

$$P_{motor} = \frac{F_{wheel} v}{\eta_{gear}} \tag{5.2}$$

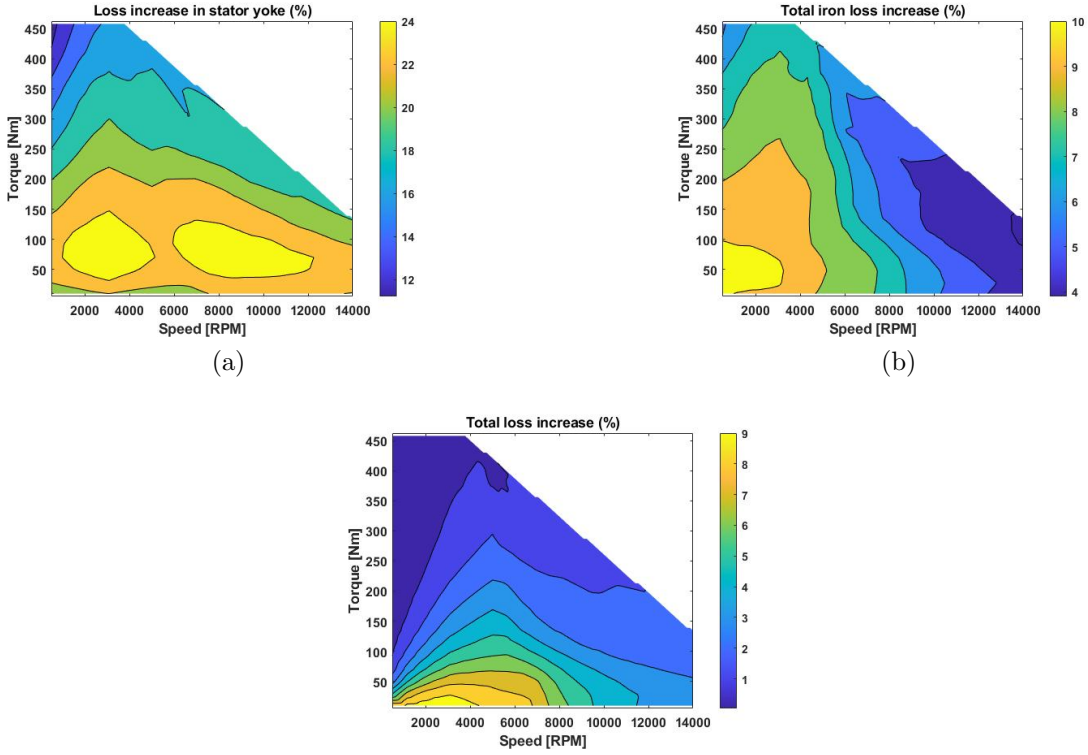

Figure 5.9: (a) Stator yoke iron loss, (b) total iron loss and (c) total loss increase (%) for Case A

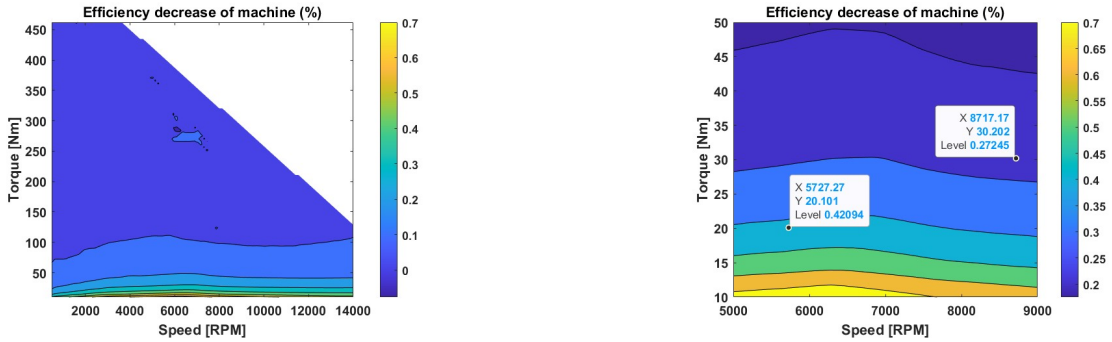

Figure 5.10: Decrease in machine efficiency in Case A for (a) entire operation range and (b) specific range

$$n_{motor} = \frac{60v}{\pi D_{wheel}} k_{gear} \tag{5.3}$$

$$T = \frac{60 P_{motor}}{2\pi n_{motor}} \tag{5.4}$$

where F_{wheel} is the total force from the wheels of the vehicle to the ground, ρ_{air} is air density (1.225 kg/m^3), v is vehicle velocity, g is the gravitational constant (9.82), α

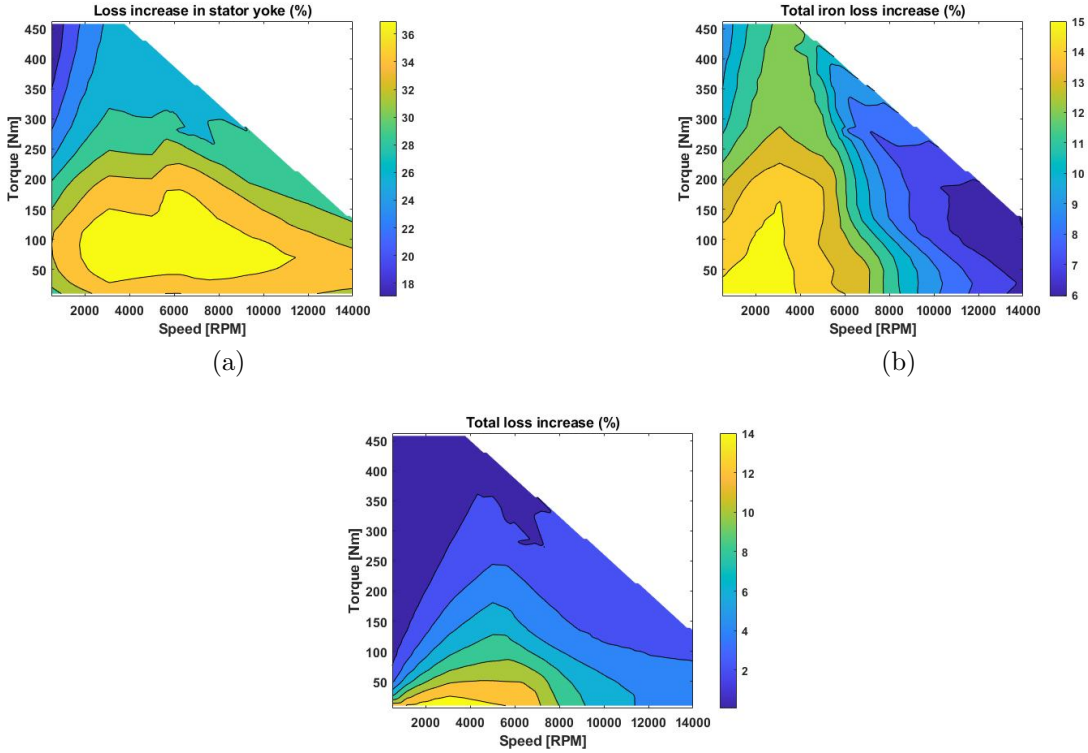

Figure 5.11: (a) Stator yoke iron loss, (b) total iron loss and (c) total loss increase (%) for Case B

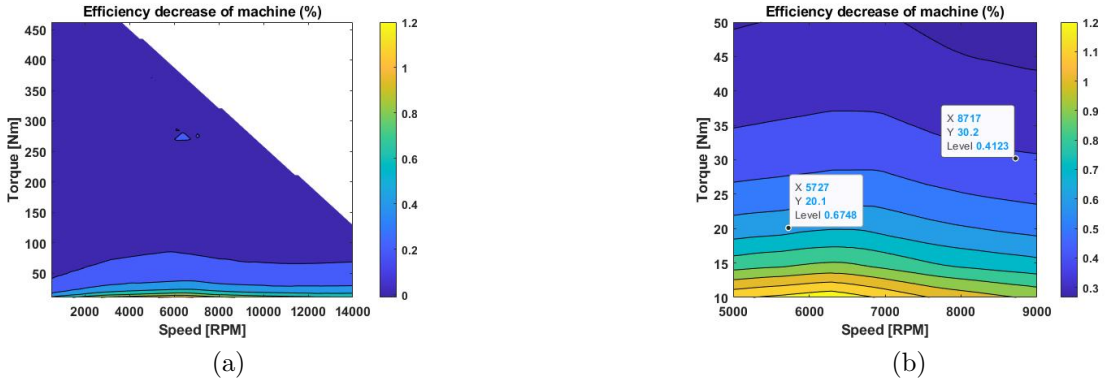

Figure 5.12: Decrease in machine efficiency in Case B for (a) entire operation range and (b) specific range

is the inclination angle (selected as 0°), n_{motor} is rotor speed and T is machine torque.

The average efficiency of the drive cycle was determined by comparing the total transmitted power and power loss of the operation points, using the $T\omega$-map generated in JMAG (Figure 5.5). In Figure 5.14, the calculated operation points of the drive cycle are shown.

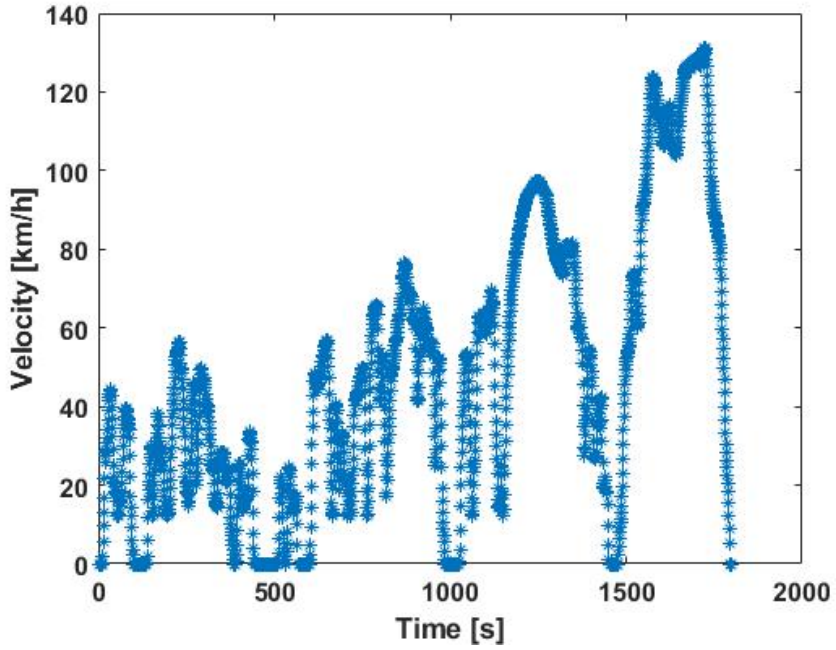

Figure 5.13: WLTC-CL3 drive cycle

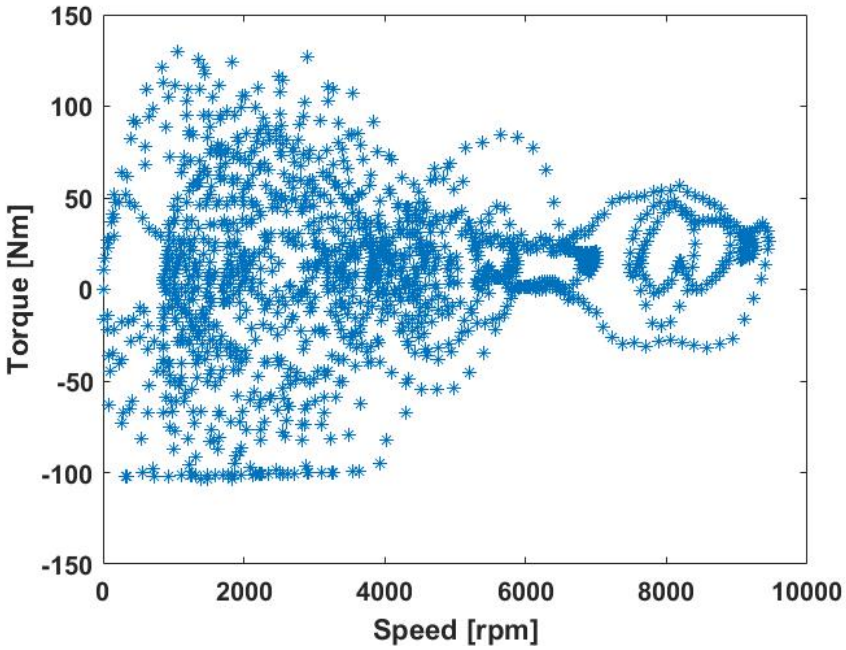

Figure 5.14: Operation points of motor of example vehicle using WLTC-CL3 drive cycle

Average efficiency of the motor for the drive cycle is presented in Table 5.5. The results show a 0.53% decrease in efficiency for Case A as compared to the case with no stress and a 0.83 % efficiency decrease for Case B. It can be observed that the decrease in efficiency for the drive cycle is significant even at a lower stress, as seen

in case A, but that the change in efficiency between case A and case B was not as large, similarly to what was seen for the specific operation points studied in Figure 5.12.

Table 5.5: Efficiency of drive cycle

Case	Efficiency [%]
No Stress	91.01
A	90.48
B	90.18

From the results, it is clear that the joint fit between housing and stator has a large impact on the performance of the machine, especially at lower torque, which is extra crucial since rotating machines normally operate at low torque in most vehicles, as the results from the drive cycle showed.

6
Discussion

6.1 Previous frame version and current frame issues

The development of the custom frame underwent three different versions. The initial version (see Appendix B.1) suffered from an erroneous estimation of the magnitude of compressive stress. It utilized acrylic as construction material and was assembled using acrylic glue. However, simple tests revealed that the acrylic material exhibited insufficient strength. Under applied compressive stress, the entire frame would become structurally compromised and prone to complete failure. It became evident that acrylic was not a wise choice of material. Nevertheless, exploring the use of acrylic material provided valuable insights for the subsequent development of the frame.

The second version (see Appendix B.2) closely resembled the final version in terms of its overall design. Recognizing that the frame needed to withstand forces of approximately 100 kg, the second version employed 3D printing and the strongest available ABS material. The frame base and some smaller components, however, remained composed of acrylic material. Test results showed that the frame could sustain compressive stresses exceeding 60 MPa without damage, when two samples were added. Thus, the second version of the framework was shown to exhibit sufficient material strength.

Upon conducting tests connected to the Brockhaus equipment, the experimental data indeed demonstrated significant variations in permeability and losses of Fe-3% Si steel with increasing compressive stress. However, the test results for the samples in their natural state (compressive stress = 0) were not satisfactory compared to the standard SST results. Under the stress-free condition, the B-H curves obtained using the custom fram exhibited noticeable elongation outward and total losses significantly exceeding the standard values. This discrepancy could likely be attributed to the selection of the yoke material. In our frame, stacked layers of Fe-3% Si steel were used as the yoke, whereas the standard SST employed a ferromagnetic material. This choice resulted in a higher proportion of losses occurring in the steel sheets used to complete the magnetic circuit. The stacked configuration of the steel sheets also introduced additional air gaps, leading to increased magnetic leakage. The combination of these factors contributed to the appearance of additional losses in the second version of the custom frame.

The third and final version, based on the second version(see Appendix B.3), incorporated a ferromagnetic yoke and changed the sample orientation from horizontal to vertical. From the test results, it was observed that the issue of additional losses had been successfully resolved, and the test results in the stress-free state were consistent with the standard SST. However, the frame still exhibited some issues. The main problem arose when the B-H curves reached the high magnetic field intensity range, where the saturation trend of the curves was less pronounced compared to the standard SST curves. This resulted in lower magnetic field intensities corresponding to the high flux density, making it difficult to obtain valid results in FEM simulations. To address this, we extrapolating values from 0.1 to 1.6 T, where material saturation is taken into consideration to get H-values for higher excitation levels. It is currently unclear whether this issue is inherent to the framework design or a result of the testing equipment. This is a matter that warrants further investigation in future studies.

6.2 Stress distribution in JMAG

The sample machine used in JMAG is a simplified, 2D model of a rotating machine. As such, stress distribution generated in the stator is generated for one plane, or slice, of the machine, while in reality stresses generated by press fit or shrink fit vary in the machine from the drive end to the other end. The two cases presented in the thesis give an indication of the impact of joint fit on machine performance at two different slices of a rotating machine (one where stress is lower and one where stress is higher). Furthermore, the design used here is no official design and the material used was degraded even before applying stresses to it. Therefore, loss distribution as impacted by joint fit could be different in an official machine design.

Both shrink fit and press fit was tested in JMAG, where the stress distribution generated by press fit depends on the interference between the housing and stator, and shrink fit depends on the temperature load of the housing (and thermal expansion of the housing material). Since tensile stresses were not analysed and compressive stress is applied in the same direction by shrink fit and press fit, the only clear difference between applying press fit or shrink fit to the stator was in the scaling of stress magnitude (i.e. interference or temperature). A method of joining stator housing to stator is press fitting the housing to stator at 20 °C and then cooling the stator housing to apply shrink fit, which was done in Case B. Based on the results however, it seems that press fitting with higher interference between stator and housing would generate the same or similar results. More research in regards to exactly how JMAG calculate stresses due to constraints placed on the stator is needed to evaluate this further however.

6.3 Ethics and sustainability

The worldwide transition from combustion motors to electric motors is one of many transitions done to reduce pollution and pursue a sustainable society. Improving the efficiency of today's electric motors is therefore crucial in order to ensure a smooth transition. This thesis has been dedicated to measuring the effects of compressive stress, which is one factor that is affecting electric motor efficiency, so that compressive stress can be considered in future designs of electric motors. The idea is that this will help improve the overall efficiency of future motors, and thus aid in the pursuit of a sustainable society. The thesis is also ethically motivated since the transition to electric motors is done in order to do the right thing for the environment and all those living in it. There are many who are left exposed to the ongoing climate change, which means that it is the responsibility of all of us to do what we can to help.

6.4 Future works

A future work identified in this thesis is the separation of loss components and developing expressions for each component coefficient as function of excitation level and stress. The custom frame developed in this thesis can be utilized for this purpose. The frame can be run with DC excitation where all measured losses can be assumed to hysteresis losses and eddy losses can be analytically calculated from (2.2) for lower frequencies where flux density is uniform throughout the samples. Also, testing the custom frame with other electrical steel materials is necessary to study the behavior at higher excitation level where the material should saturate to see if the lack of material saturation in the measurements are due to the frame, or if it was due to the degradation of the test material.

Another future work is the continuation of analysing the effects of interference fits between housing and stator, as the custom frame can be utilized for studying other electric steel samples, or the stress values obtained here can be used in 3D-models representing the actual motors used, where the modeled stress distribution is closer to the actual stress distribution in the actual motor.

A final future work is to also study effects of tensile stresses on electrical steel materials. This was not done here, due to the required complexity of the design to make this possible. Compressive stress has a more significant impact on losses due to joint fit, since the magnitude of compressive stress is higher and loss increase due to compressive stress is higher in electrical steel materials. Tensile stresses in the stator will still have an impact however, and are necessary to analyse in order to increase the accuracy of the modeled loss distribution in the stator.

7
Conclusion

The summarised findings from the effects of compressive stress on non-oriented electrical steel are as follows:

- As compressive stress is applied, induction strength of non-oriented electrical is reduced as permeability of the material at excitation levels below the saturation region is heavily reduced. As compressive stress exceeds 35 MPa, peak permeability of the material is achieved already at 0.2 - 0.3 Tesla excitation and permeability at higher excitation levels barely show a frequency dependency anymore.

- The shape of the hysteresis loops of the material change as magnetization is pushed to much higher fields, increasing hysteresis and excess losses of the material. Measured material loss increase peaked at 74.88 % at compressive stress of 60.6 MPa and frequency of 1000 Hz. For frequencies higher than 50 Hz and compressive stress higher than 10.3 MPa, loss increase was higher than 15 % at all excitation levels.

- At compressive stress higher than 35.2 MPa, effects of compressive stress shows a saturating trend as increasing stress show less of an impact. At higher frequencies (1000 Hz was tested), this saturating effect is damped and the impact of further increased stress is higher. Furthermore, at lower compressive stress, the % increase in losses was higher for lower frequencies and at higher compressive stress, the % increase was higher for higher frequencies.

The summarised findings from the FEM-simulations are as follows:

- A joint fit, called Case A, generating approximately 15 - 17 MPa of compressive stress in most of the stator yoke resulted in an efficiency decrease of up to 0.74 % in the machine's operation range

- A joint fit, called Case B, generating approximately 30 - 31 MPa of compressive stress in most of the stator yoke resulted in an efficiency decrease of up to 1.27 % in the machine's operation range

- Effects on efficiency are higher at low torque, where the machine is normally operated. At an operation point approximately corresponding to 80 km/h when the motor is operated in a vehicle, efficiency decrease was 0.42% and 0.67

%, for Case A and B respectively. At another operation point approximately corresponding to 120 km/h, efficiency decrease was 0.27% and 0.41%, for Case A and B respectively

Bibliography

[1] European Parliament, "Fit for 55: zero CO2 emissions for new cars and vans in 2035," 2 2023. [Online]. Available: https://www.europarl.europa.eu/news/en/press-room/20230210IPR74715/fit-for-55-zero-co2-emissions-for-new-cars-and-vans-in-2035

[2] Dr James Edmondson and Luke Gear, "IDTechEx: Electric Motors for Electric Vehicles 2022-2032," *IDTechEx*, 2022.

[3] Zhenyu G and Li L, "High grade non-oriented electrical steel technology development and application technology," *Angang Technology*, vol. 2, pp. 6–10, 2011.

[4] Fengxi L, "Domestic and international electrical steel market research," *Wuhan Iron and Steel Corporation Technology*, vol. 38, no. 3, pp. 55–57, 2000.

[5] Chuhua Z and Qianghua P, "Changes in the magnetic domain structure of silicon steel sheets under static load," *Nondestructive Testing*, vol. 33, no. 7, pp. 11–14, 2011.

[6] Y. Hayakawa, "Electrical Steels," *Encyclopedia of Materials: Metals and Alloys*, pp. 208–213, 9 2021.

[7] O. Perevertov and R. Schäfer, "Magnetic properties and magnetic domain structure of grainoriented Fe-3%Si steel under compression," *Materials Research Express*, vol. 3, no. 9, 9 2016.

[8] O. Perevertov, "Influence of the applied elastic tensile and compressive stress on the hysteresis curves of Fe-3%Si non-oriented steel," *Journal of Magnetism and Magnetic Materials*, vol. 428, pp. 223–228, 4 2017.

[9] B. A. Nasir, "An Accurate Iron Core Loss Model in Equivalent Circuit of Induction Machines," *Journal of Energy*, vol. 2020, 2020.

[10] D. Kowal, P. Sergeant, L. Dupre, and L. Vandenbossche, "Comparison of iron loss models for electrical machines with different frequency domain and time domain methods for excess loss prediction," *IEEE Transactions on Magnetics*, vol. 51, no. 1, 2015.

[11] G. Bertotti, "GENERAL PROPERTIES OF POWER LOSSES IN SOFT FERROMAGNETIC MATERIALS." *IEEE Transactions on Magnetics*, vol. 24, no. 1, 1987.

[12] D. Singh, P. Rasilo, F. Martin, A. Belahcen, and A. Arkkio, "Effect of Mechanical Stress on Excess Loss of Electrical Steel Sheets," *IEEE Transactions on Magnetics*, vol. 51, no. 11, 2015.

[13] G. Bertotti, D. Chiarabaglio, F. Fiorillo, A. Boglietti, M. Chiampi, and M. Lazzari, "An improved estimation of iron losses in rotating electrical machines," *IEEE Transactions on Magnetics*, vol. 27, no. 6, 1991.

[14] International Electrotechnical Commission, *Magnetic materials. Part 2, Methods of measurement of the magnetic properties of electrical steel strip and sheet by means of an Epstein frame.* [Online]. Available: https://webstore.iec.ch/publication/62746

[15] International Electrotechnical commission, *Magnetic materials. Part 3: Methods of measurement of the magnetic properties of electrical steel strip and sheet by means of a single sheet tester.* [Online]. Available: https://webstore.iec.ch/publication/66641

[16] F. Müller, G. Bavendiek, B. Schauerte, and K. Hameyer, "Measurement and simulation of a rotational single sheet tester," *Archives of Electrical Engineering*, vol. 68, no. 1, 2019.

[17] L. Bernard and L. Daniel, "Effect of stress on magnetic hysteresis losses in a switched reluctance motor: Application to stator and rotor shrink fitting," *IEEE Transactions on Magnetics*, vol. 51, no. 9, 2015.

[18] Y. Kai, Y. Tsuchida, T. Todaka, and M. Enokizono, "Evaluation of local residual stress distribution of stator core in a rotating machine," *Electrical Engineering in Japan*, vol. 181, no. 3, 2012.

[19] L. Bernard, X. Mininger, L. Daniel, G. Krebs, F. Bouillault, and M. Gabsi, "Effect of stress on switched reluctance motors: A magneto-elastic finite-element approach based on multiscale constitutive laws," *IEEE Transactions on Magnetics*, vol. 47, no. 9, 2011.

[20] K. Yamazaki, H. Mukaiyama, and L. Daniel, "Effects of multi-axial mechanical stress on loss characteristics of electrical steel sheets and interior permanent magnet machines," *IEEE Transactions on Magnetics*, vol. 54, no. 3, 2018.

[21] H. Hüyük, O. Music, A. Koç, Karadoan, and Bayram, "Analysis of elastic-plastic interference-fit joints," in *Procedia Engineering*, vol. 81, 2014.

[22] Interplex, "Press-Fit: Understanding the Technology, its Advantages and Applications," 10 2020. [Online]. Available: https://interplex.com/press-fit-guide/

[23] Z. Huiyan, Z. Junjie, and Z. Lihua, "Study on the effect of compressive stress on magnetic properties of silicon steel sheets," *JOURNAL OF HEBEI UNIVERSITY OF TECHNOLOGY*, vol. 50, no. 4, pp. 10–16, 2021.

[24] Xiaojun Z and Lingyun Z, "Experimental Study on the Effect of Mechanical Stress on the Comprehensive Magnetic Properties of the Grain-Oriented Silicon Stee," *TRANSACTIONS OF CHINA ELECTROTECHNICAL SOCIETY*, vol. 37, no. 22, 11 2022.

[25] A. Pulnikov, V. Permiakov, M. De Wulf, and J. Melkebeek, "Measuring setup for the investigation of the influence of mechanical stresses on magnetic properties of electrical steel," in *Journal of Magnetism and Magnetic Materials*, vol. 254-255, 2003.

[26] O. Lahyaoui, V. Lanfranchi, N. Buiron, F. Martin, U. Aydin, and A. Belahcen, "Effect of mechanical stress on magnetization and magnetostriction strain behavior of non-oriented Si-Fe steels at different directions and under pseudo-DC conditions," *International Journal of Applied Electromagnetics and Mechanics*, vol. 60, no. 2, 2019.

[27] A. P. Baghel, J. B. Blumenfeld, L. Santandrea, G. Krebs, and L. Daniel, "Effect of mechanical stress on different core loss components along orthogonal directions in electrical steels," *Electrical Engineering*, vol. 101, no. 3, 2019.

[28] O. Perevertov, J. Thielsch, and R. Schäfer, "Effect of applied tensile stress on the hysteresis curve and magnetic domain structure of grain-oriented transverse Fe-3%Si steel," *Journal of Magnetism and Magnetic Materials*, vol. 385, 2015.

[29] B. J. Mailhe, L. D. Bernard, L. Daniel, N. Sadowski, and N. J. Batistela, "Modified-SST for Uniaxial Characterization of Electrical Steel Sheets under Controlled Induced Voltage and Constant Stress," *IEEE Transactions on Instrumentation and Measurement*, vol. 69, no. 12, 2020.

[30] Deepak Singh, "Effect of Stress on Magnetic Properties of Electrical Steel Sheet and Core Losses in Electrical Machines," Ph.D. dissertation, Aalto University, Helsinki, 2016.

[31] Tata Steel, "Tata Steel Hi-Lite Electrical Steel NO25-1350H Data Sheet." [Online]. Available: https://www.tatasteeleurope.com/sites/default/files/tata-steel-hi-lite-electrical-steel-no25-1350h-datasheet-en.pdf

[32] RS PRO, "RS PRO Alloy Steel S Beam Tension Load Cell," 2022. [Online]. Available: https://se.rs-online.com/web/p/strain-gauges/2042768

[33] Brockhaus Measurements, "Electrical Steel Tester MPG 200," 2023. [Online]. Available: https://www.brockhaus.com/measurements/products/softmagnetic/est-series/mpg-200/?lang=en

[34] JSOL Corporation, "JMAG Application Note Iron Loss Analysis of an IPM Motor Including the Effect of Shrink Fitting CONTENTS," Tech. Rep.

[35] Comsol, "COMSOL Multiphysics Application Library," Tech. Rep., 2021. [Online]. Available: www.comsol.com/trademarks.

A

Appendix 1

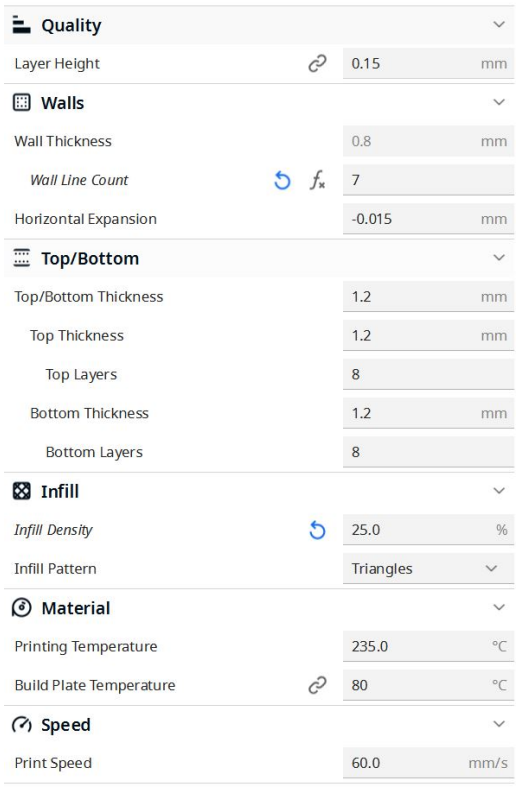

(a) 3D printer parameter setting-1

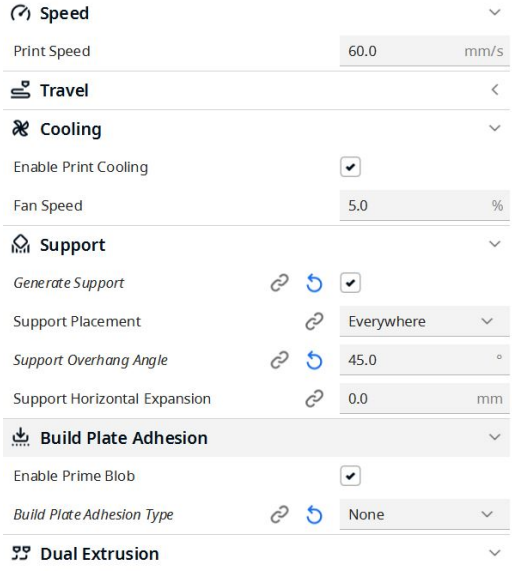

(b) 3D printer parameter setting-2

Figure A.1: 3D printer parameter setting

B

Appendix 2

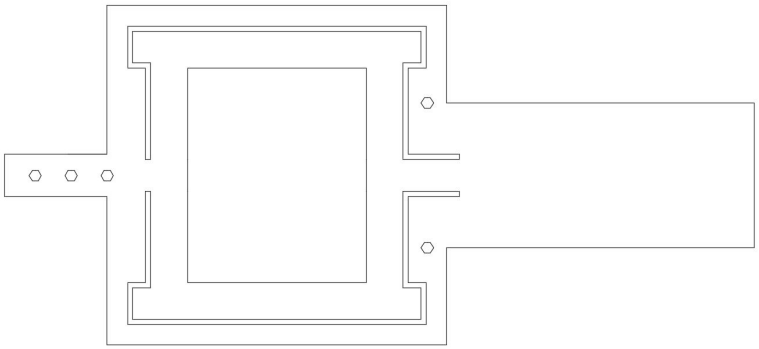

(a) 2D Design

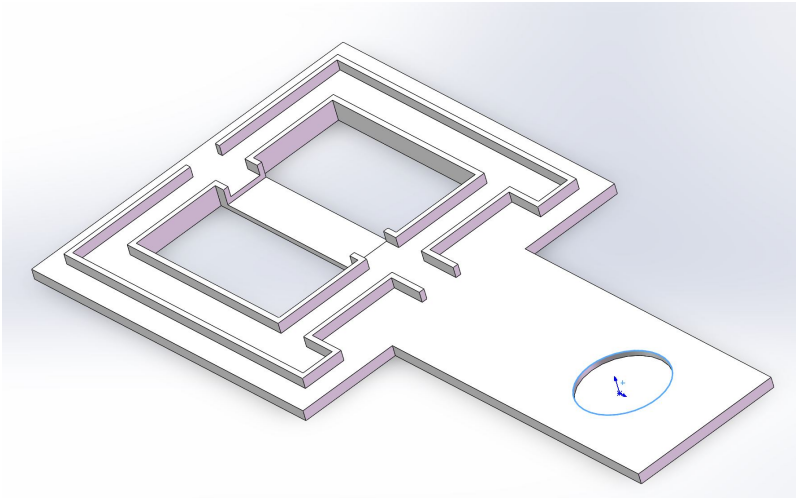

(b) 3D Design

Figure B.1: Design of frame Ver1.0

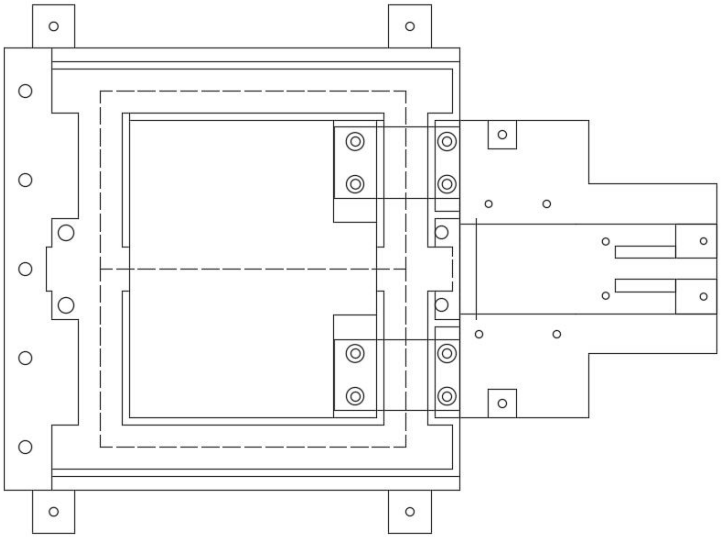

(a) 2D Design

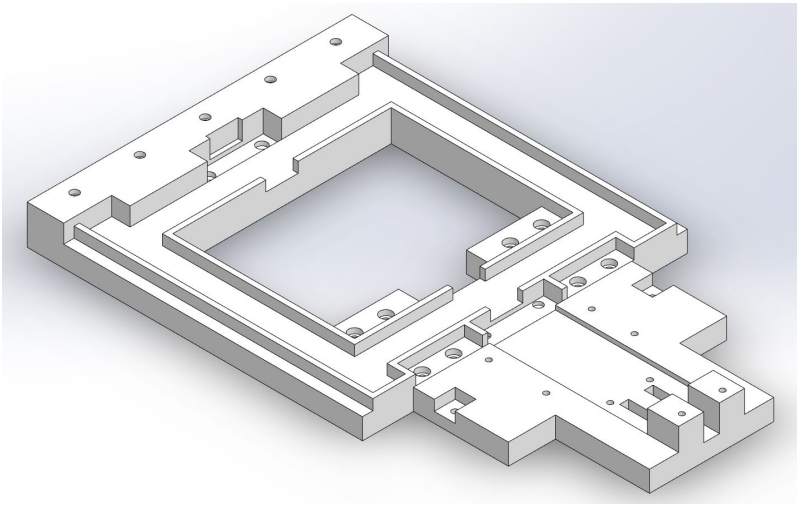

(b) 3D Design

Figure B.2: Design of frame Ver2.0

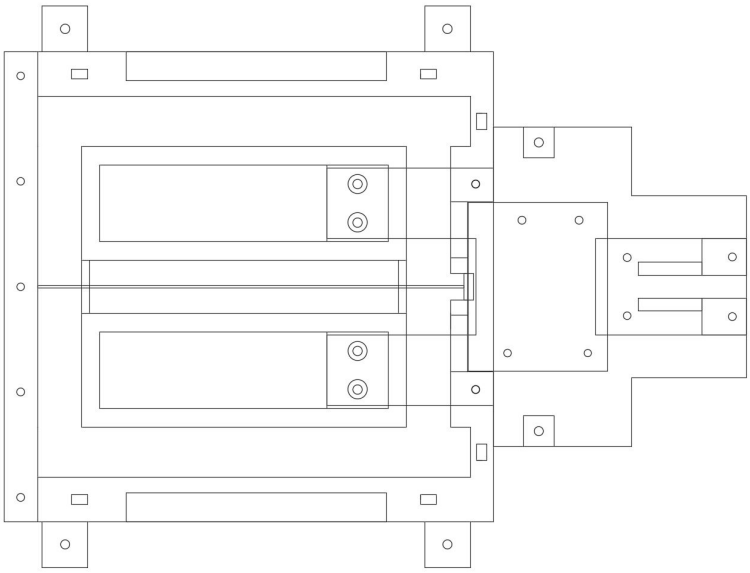

(a) 2D Design

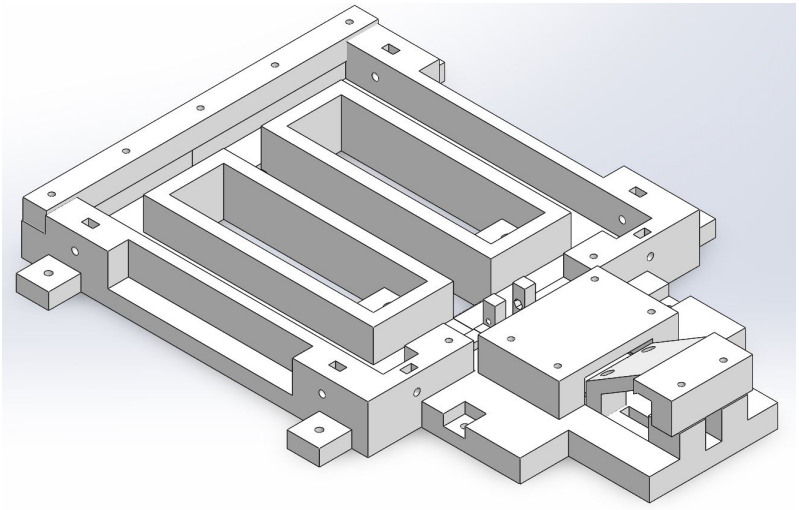

(b) 3D Design

Figure B.3: Design of frame Ver3.0

C

Appendix 3

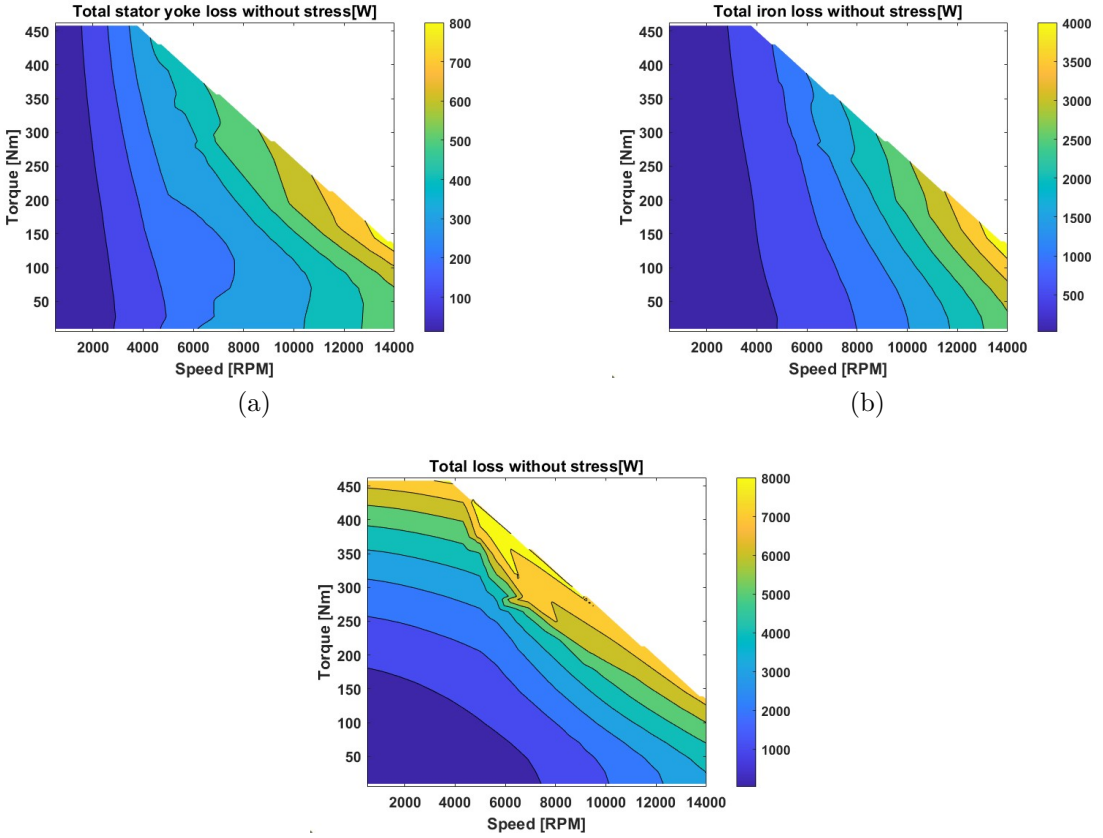

(a) (b) (c)

Figure C.1: (a) Stator yoke iron loss, (b) total iron loss and (c) total loss of IPM without stress

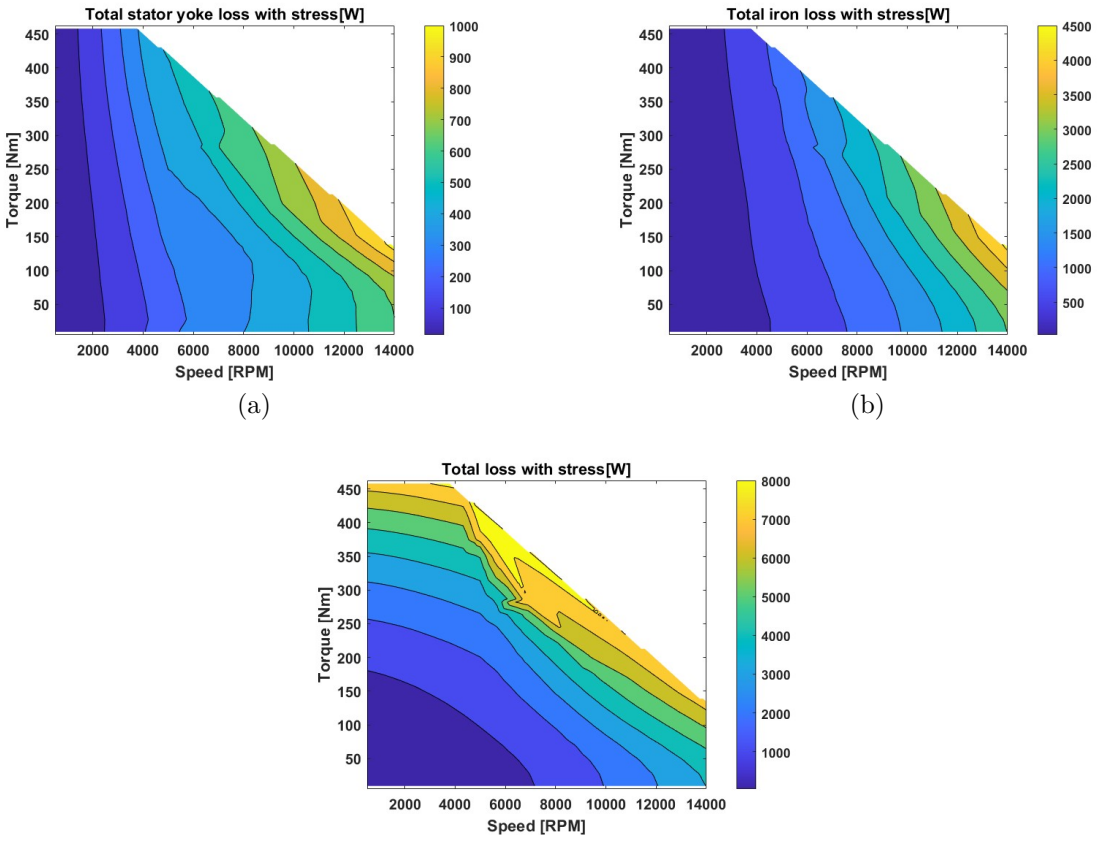

Figure C.2: (a) Stator yoke iron loss, (b) total iron loss and (c) total loss of IPM for Case A

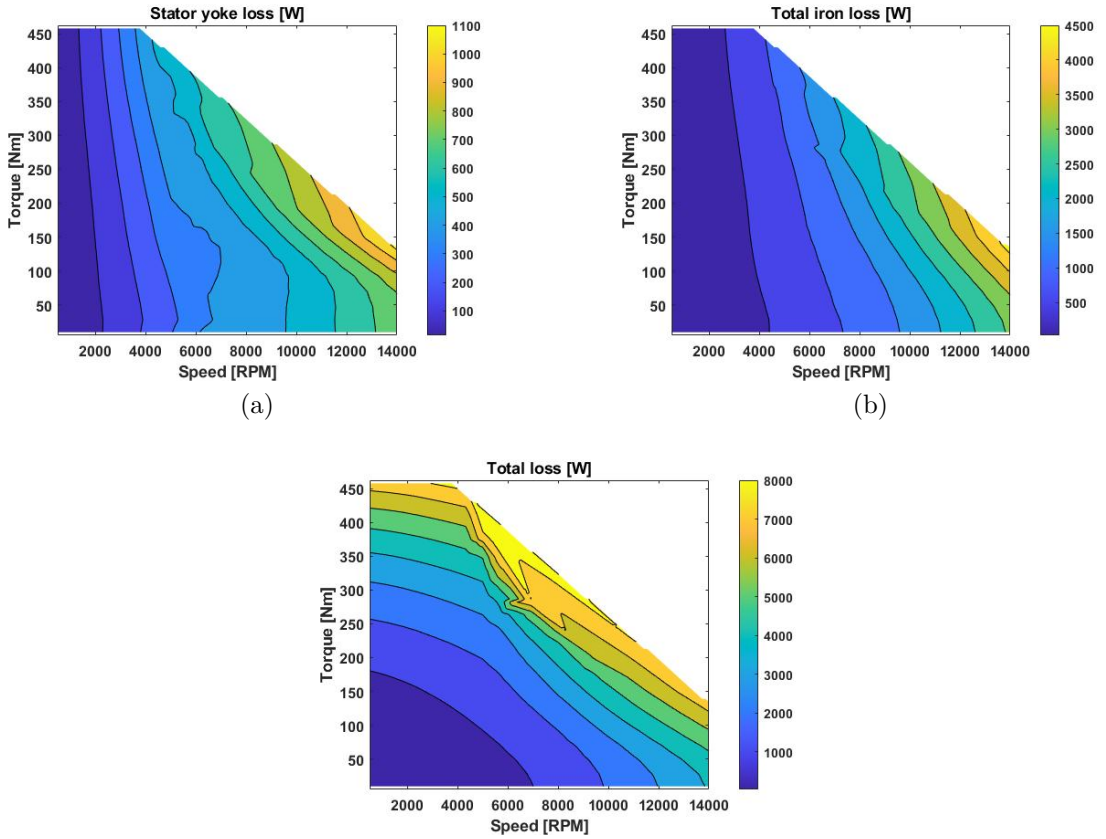

Figure C.3: (a) Stator yoke iron loss, (b) total iron loss and (c) total loss of IPM for Case B

DEPARTMENT OF ELECTRICAL ENGINEERING
CHALMERS UNIVERSITY OF TECHNOLOGY
Gothenburg, Sweden
www.chalmers.se

CHALMERS
UNIVERSITY OF TECHNOLOGY